MEDICAL ISOTOPE PRODUCTION REACTOR

Reactor design for a small sized
Aqueous Homogeneous Reactor for producing
molybdenum-99 for regional demand

NERA-131-2013-005
M.V. Huisman
3 July 2013

Medical Isotope Production Reactor

Reactor design for a small sized Aqueous Homogeneous Reactor for producing molybdenum-99 for regional demand

NERA-131-2013-005

Delft
3 July 2013

M.V. Huisman
Master Thesis Applied Physics
1357964

Supervisors
Dr. Ir. Jan-Leen Kloosterman
Dr. Ir. Martin Rohde

Committee
Dr. Ir. Jan-Leen Kloosterman†
Dr. Ir. Martin Rohde†
Dr. Ir. Luis Portela‡
† NERA, AS, TU Delft
‡ TP, AS, TU Delft

Delft University of Technology
Faculty of Applied Sciences
department of
Radiation Science and Technology
section
Nuclear Energy and Radiation Applications

Abstract

An Aqueous Homogeneous Reactor (AHR) is an ideal candidate to use as a Medical Isotope Production Reactor (MIPR) for the production of molybdenum-99 (^{99}Mo) and other medical isotopes. The benefits of an AHR are the size, the total power and the strongly negative temperature feedback.

In this thesis, the focus is on the design and safety characteristics of the MIPR. Since no known benchmark or outline is available, several geometries were assessed. The core volume of the studied configuration is around 40 L depending on the layout of the internal structural materials. The different geometries were tested using the same mass flow rate to assess their capability of heat removal. The best performing geometry is the so called *Bulkheads*, which consist of four inlets and one outlet. The benefit of this configuration is the smooth flow of the fuel (uranium salt and water) through the system. Furthermore no obstruction for the radiolytic gases is present. The assessed geometries with a single inlet require more structural material to achieve the same heat removal than the *Bulkheads* geometry. The drawback of the extra structural material is that radiolytic gases can get trapped inside the reactor (depending on the design) and vortices may appear leading to hot spots.

The mass flow rate of the system was also optimized to find the maximum total power and power density. The maximum mass flow rate was found to be $0.5\,\mathrm{kg\,s^{-1}}$. Above this value the maximum power density exceeds $2.5\,\mathrm{MW\,m^{-3}}$ in which region the behavior of an AHR is unknown.

The *Bulkheads* geometry uses 20 % enriched uranyl nitrate as fuel. The concentration of the fuel is $248\,\mathrm{g\,U\,L^{-1}}$, in total 10.9 kg uranium is dissolved in the system. The total power of the system is 42.2 kW, which leads to a weekly ^{99}Mo production of 309 6-day Ci. This is equal to 2.5 % of the weekly world demand. Since the total power of the reactor is relatively low, the consumption of uranium is low as well, therefore the system can be operated for long periods without refueling.

The safety characteristics were also tested, a low calculated temperature feedback coefficient of $-2.814\,\mathrm{pcm\,K^{-1}}$ has been calculated, the system was found to be rather sensitive to both the uranium concentration and reactivity insertions. However, the fuel inside the reactor will not start to boil when the heat exchanger fails despite the low temperature feedback coefficient. In case of a fission product filter failure, the xenon-135 concentration in the reactor will slowly increase leading to a decrease in the total power. Other research shows temperature feedback coefficients ranging from $-200\,\mathrm{pcm\,K^{-1}}$ to $-90\,\mathrm{pcm\,K^{-1}}$ for different enrichment, concentrations and uranium slats. This means that an AHR can be even more stable then reported in this research.

Table of contents

Chapter 1

Introduction

In the medical field, several isotopes are used as a radioactive tracer for making body scans. The most commonly used medical isotope is technetium-99m (^{99m}Tc). Since ^{99m}Tc has a short half-life of 6.0058 hours, a stock pile cannot be produced. Therefore molybdenum-99 (^{99}Mo) is delivered to the medical centers, because ^{99}Mo is the parent radioisotope of ^{99m}Tc. When the ^{99m}Tc is needed, it can be extracted from the ^{99}Mo by so called Technetium-99m generators.

1.1 Conventional method of molybdenum-99 production

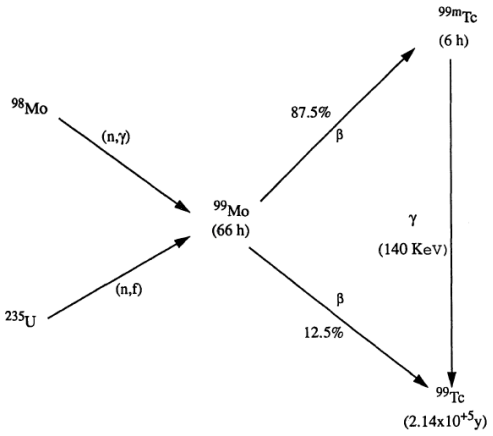

Figure 1.1: Production and decay of ^{99}Mo and ^{99m}Tc[1].

The current way to produce ^{99}Mo is by irradiating high enriched uranium (HEU) or low enriched uranium (LEU) targets with a high neutron flux in a nuclear reactor (see fig. 1.1). After being irritated for a couple of days in the reactor, the targets are brought to the reprocessing facility. Here, the ^{99}Mo is extracted and shipped to the medical centers.

The production of ^{99}Mo is expressed in 6-day Ci. The unit Curie (Ci) is an old unit of activity, but is still used to express the radioactivity of ^{99}Mo. In other fields of study, Curie has been replaced by Becquerel (Bq). The conversion between the two units is:

$$1\,\mathrm{Ci} = 3.7 \times 10^{10}\,\mathrm{Bq}.$$

The prefix "6-day" represent the activity of ^{99}Mo having left the production facility for 6 days.

The weekly world demand[2] of ^{99}Mo is 12 000 6-day Ci, is produced in a few reactors:

NRU Chalk River, Canada, date of construction: 1957;
BR-2 Mol, Belgium, date of construction: 1961;
HFR Petten, the Netherlands, date of construction: 1961;
Osiris Saclay, France, date of construction: 1964;
Safari-1 Pelindaba, South Africa, date of construction: 1965,
OPAL Sydney, Australia, date of construction: 2007.

These reactors have a combined market share that exceeds 95 %, but in the last few years the two biggest production facilities, NRU and HFR, were both not operational for several months. These shutdowns have had a major impact on the supply of ^{99}Mo. Since ^{99}Mo has a half-life of 66 hours, a stock pile cannot be produced.

Figure 1.2: The current locations of the production facilities of ^{99}Mo around the world[3].

1.2 Conceptual method of molybdenum-99 production

The worldwide demand for molybdenum-99 (^{99}Mo) as medical isotope will increase in the near future[2], mainly due to increasing demand from Brazil, Russia, India and China. Therefore in 1992, Ball[4][5] described how an Aqueous Homogeneous Reactor (AHR) could be used to produce medical isotopes. When an AHR is used to produce medical isotopes, the term Medical Isotope Production Reactor (MIPR) is applied.

An AHR is a type of reactor where uranium salts are dissolved in water. The fuel is a mix consisting of the coolant (i.e. water), the moderator(i.e. water) and the uranium salt, hence the name "homogeneous". The comparison with a molten salt reactor is often made, due to fact that the fuel is also a liquid. The strong negative temperature reactivity feedback coefficient[6] makes an AHR more stable than conventional reactors. Other positive aspects of an AHR are its small size and low total power. However an AHR cannot be used to produce electrical power, because the fuel should never boil, otherwise the concentration will increase due to the evaporation of the water and the system stays no longer critical.

With an AHR also other isotopes can be extracted from the solution besides ^{99}Mo. These isotopes includes, ^{89}Sr which is used for the treatment of bone cancer and ^{131}I which is used for treatment of thyrotoxicosis (hyperthyroidism) and some types of thyroid cancer. ^{133}I decays to ^{133}Xe by beta-decay within 20.8 hours, ^{133}Xe can be used for imaging of the lungs. ^{135}Xe is known as a neutron absorber and is therefore undesirable in the reactor.

1.3 Early Aqueous Homogeneous Reactor

The first homogeneous liquid-fuel reactor ever built was the LOPO reactor[7] at the Los Alamos National Laboratory. This so called LOw POwer reactor was constructed in 1943 and it became the third reactor ever build after Fermi's "pile" at Chicago's Stagg Field and the X-10 graphite reactor at Oak Ridge National Laboratory. To deceive the enemy intelligence, the code name "Water Boiler" was given to the LOPO reactor. In this reactor water did not boil, but hydrogen and oxygen gas were formed. The aim of the research was

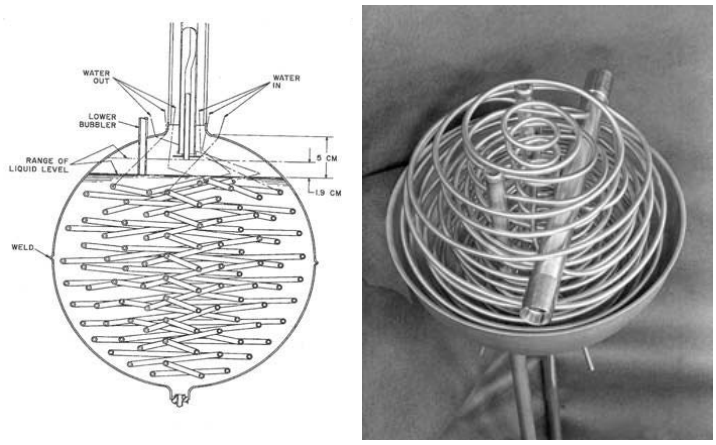

(a) Cross section (b) Cutaway view

Figure 1.3: The SUPO reactor at Los Alamos National Labatory. The spiral tubing is the cooling system and the big tubes are the control rod guide tubes. The diameter of the spherical vessel is 30.48 cm[8].

to verify critical-mass calculations and to measure the fission, neutron capture and scattering cross sections of various materials. In May 1944, LOPO reactor achieved criticality with a fule containing 14 % enriched uranyl sulphate.

After the achievement of criticality, the LOPO reactor was replaced by the HIgh POwer reactor (HYPO). Instead of using uranyl sulphate solution as fuel, an uranyl nitrate solution was used. HYPO became operational in December 1944 and was used for validating critical mass calculations and measuring cross sections for the early atomic bombs. The HYPO reactor received an upgrade in March 1951 and became the SUPO reactor (SUper POwer). This was done by increasing the enrichment to 88.7 %, by improving the cooling system and by installing a gas recombination system to remove the hydrogen and oxygen gases. The system operated until 1974 and was mostly used as a neutron source. A cross section and a cutaway view of the system can be seen in respectively fig. 1.3(a) and fig. 1.3(b). Imperial College Londen[9] presented a model for the coupled neutronic and fluid time dependent characteristics of the SUPO reactor, however investigation of the production capacity of the SUPO reactor for ^{99}Mo has not been performed.

In the early fifties, many different AHRs were built throughout the world[11]. Most of these reactors were only operational for a few years. The power levels ranged from 5 W to 50 kW and the enrichment of the uranium sulphate ranged from 20 % to 90 %. For instance KEMA build an Aqueous Homogeneous Suspension Reactor (AHSR) in the early seventies in Arnhem. This reactor differs from an AHR in the sense that it used suspended uranium dioxide particles. It operated for a few years and was then decommissioned[10].

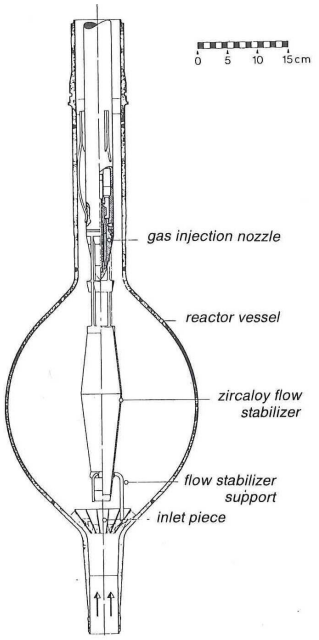

Figure 1.4: A profile of the Aqueous Homogeneous Suspension Reactor[10]. The uranium dioxide particles flow from bottom to top, the flow stabilizer ensures a smooth flow through the sphere.

One of the classical photographs of the early days of nuclear reactor can be seen in fig. 1.5. This reactor is the Homogeneous Reactor Test (HRT) located at the Oak Ridge National Laboratory[12]. The fuel consisted of an uranyl sulfate solution containing 10 grams of enriched uranium per kilogram of heavy water. It was used to convert thorium into ^{233}U using ^{235}U as the neutron source. The flow rate of the fuel was $1450\,\mathrm{L\,min^{-1}}$. The reactor core included an inner sphere and an outer sphere with heavy water which was used as a reflector. The HRT was operational in 1958 and 1959. In April 1958 it reached its maximumdesign power of 5 MW. Due to the acidity of the fuel, the structural material corroded and a leak appeared in the inner tank at the end of 1958. The hole was patched and the flow was altered. In 1959 the reactor was continuously run for 105 days but a new leak appeared and the HRT was shutdown.

Today, a few AHRs are still in operation, but these are not used for ^{99}Mo production. The successor of the SUPO reactor at Los Alamos National Laboratory is the SHEBA II (Solution High-Energy Burst Assembly)[13][14][15]. The system is larger than SUPO and uses uranyl nitrate (20% enrichment) or uranyl fluoride (5% enrichment) instead of uranyl sulphate. Another reactor still in use is The TRAnsient experiments Critical facilitY (TRACY) research reactor in Japan[16]. TRACY measures criticality accidents in order to acquire confirmation of criticality safety margins and for the validation of criticality, safety codes and nuclear data libraries. In these experiments the effect of an accident on the power output, radiation doses of neutrons and α-particles and emission quantities of radioactive matter is investigated. The fuel that TRACY consumes is LEU uranyl nitrate. In France, the SILENE reactor[17] was build and can be operated in a *pulse*, *free evolution* and *steady state* mode for different research purposes. During the *free evolution* mode, a control rod is removed slowly from the system. The system uses LEU uranyl nitrate as fuel.

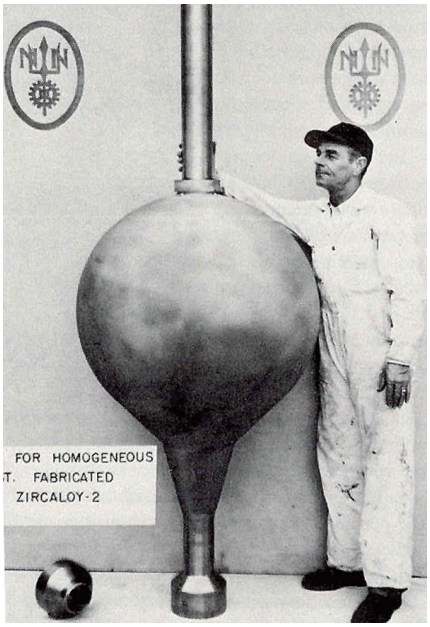

Figure 1.5: An engineer standing next to the Homogeneous Reactor Test at Oak Ridge National Laboratory. The reactor vessel is surrounded with a water reflector. The flow direction is from bottom to top. The outer diameter of the sphere is 1.52 m[12].

1.4 Recent development of Medical Isotope Production Reactors

As stated before in section 1.2, Ball described in 1992 how an AHR could be used to produce medical isotopes. For this reason The Russian Federation, the United States, Japan, France, China and Indonesia initiated programs to assess the feasibility of utilizing AHRs for the production of medical isotopes.

In 1999, the Kurchatov Institute in Moscow adapted the Argus reactor[19][20] to produce ^{99}Mo for medical diagnostics. A detailed diagram of the system can be seen in fig. 1.6. This 20 kW reactor uses HEU and LEU uranyl sulphate as fuel. The Russians have successfully produced ^{99}Mo with both fuels. The knowledge acquired from the Argus reactor has been used by the Institute of Physics and Power Engineering (IPPE) for the design of the new Solution Reactor - Radio Nuclides (SR-RN)[21]. The reactor design is almost similar to the Argus reactor, but ^{99}Mo is continuously extracted instead. The flow diagram of this system is shown in fig. 1.7.

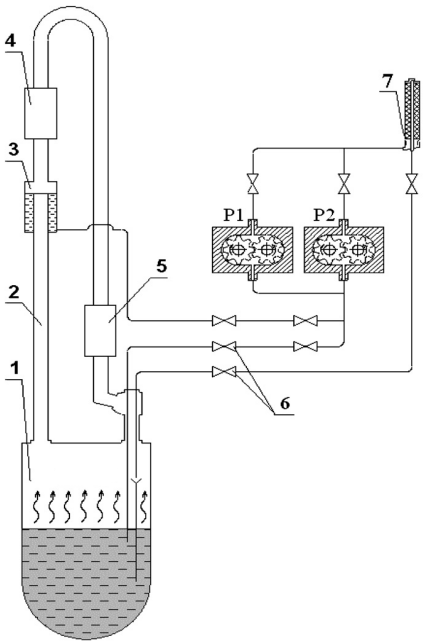

Figure 1.6: Diagram of the Argus system with the experimental loop. In the reactor vessel (1) water vapor, hydrogen and oxygen rise through the regeneration loop (2) to the heat exchanger (4). The water is collected by the condensate accumulator (3), the gases go to the catalytic recombinator (5) to be recombined to water. The secondary loop removes the ^{99}Mo from the system in the sorption column (7). The fuel is pumped around by pump P1 and P2. The diameter of the reactor vessel is 1.5 m[18].

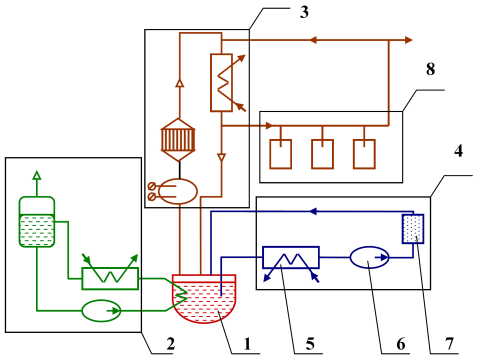

Figure 1.7: Flow diagram of the Solution Reactor - Radio Nuclides. It consist of several loops. The reactor vessel (1) is shown in red, the green loop (left of the reactor vessel) is the heat removal system (2). The blue loop (right of the reactor vessel) is the extraction loop (4) of ^{99}Mo, where (5) is the cooler, (6) is a pump and (7) the extraction column. The brown loop (above the reactor vessel) is the gas recombiner system (3). This loop can be extended to extract even more isotopes like ^{89}Sr, ^{133}Xe, (^{131}I, ^{132}I and ^{133}I). The diameter of the reactor vessel is 32 cm[21].

A detailed diagram of the MIPR designed by the Nuclear Power Institute of China is depicted in fig. 1.8. The reactor uses HEU uranyl nitrate as fuel and the fuel stays in the reactor vessel for 24 hours. Within this period, the formed gases are pumped through a strontium extractor, heat exchanger, a H_2 and O_2 recombiner and an iodine filter. After 24 hours the solution is pumped through a ^{99}Mo and an ^{131}I extractor using the low pressure tank.

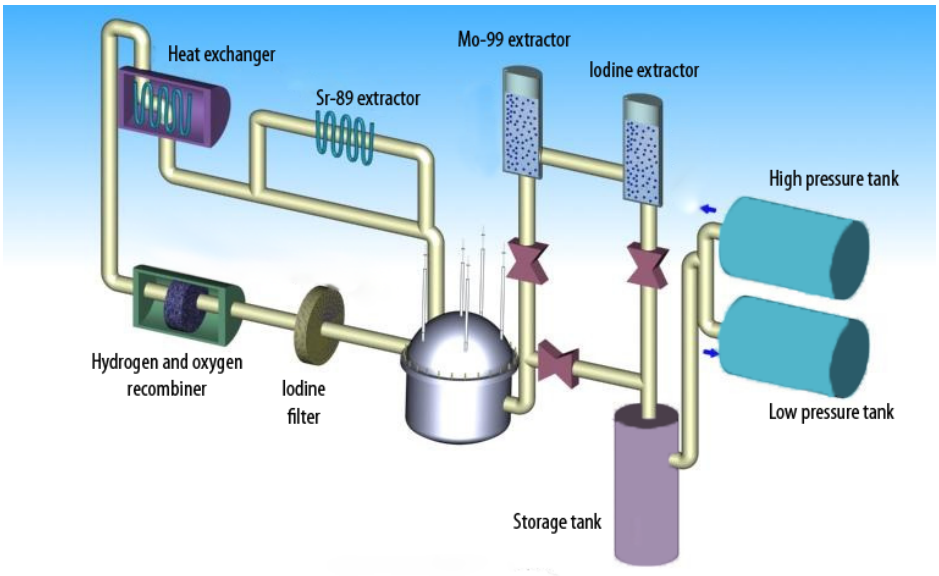

Figure 1.8: Diagram of the MIPR system, the diameter of the reactor vessel is 77 cm. The loop on the left is the gas recombiner, on the right side the ^{99}Mo and I extractor and storage tank can be seen[22].

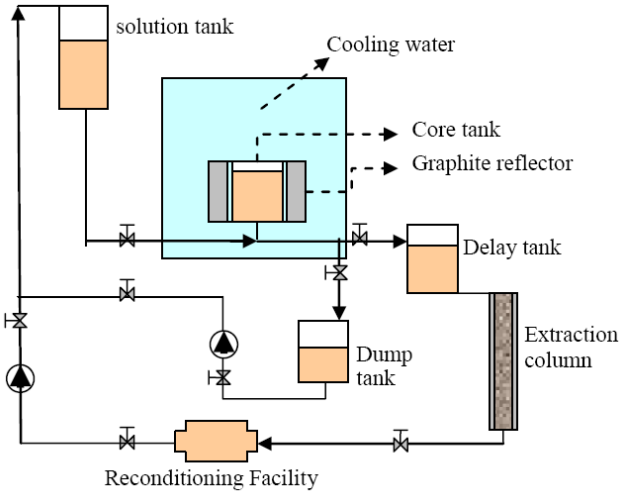

Figure 1.9: Diagram of the SAMOP system. The diameter of the reactor vessel is 15.35 cm[23]. The solution is continuously pumped around. In the delay tank short-lived isotopes will decay, in the extraction column the ^{99}Mo will be recovered. The recondition facility ensures a constant concentration of uranium and the solution tank used as a the buffer tank for the fuel.

In Indonesia, the local national nuclear energy agency (BATAN)[24][23] investigates a Sub-critical Assembly for ^{99}Mo Production (SAMOP), of which a detailed diagram is depicted in fig. 1.9. The idea is that the reactor should contain a minimal amount of ^{235}U so that an external source is required to make the reactor critical, making the reactor less vulnerable for terrorist threats. Therefore, an external source is required to make the system critical. The solution is pumped around, which implies that ^{99}Mo is extracted continuously. The delay tank is used as a buffer to allow isotopes like ^{132}I and ^{133}I to decay.

The Babcock & Wilcox Company (B&W) has plans to build a solution reactor (MIPR) in Lynchburg, Virginia[25]. The conceptual design uses a batch cycle of six days, where the solution is irritated during this period. The MIPR has the same volume and power as the MIPR in China, but uses LEU instead of HEU. Therefore the concentration of uranyl nitrate is 2.5 times higher to compensate for the lower concentration of ^{235}U in the fuel. Two design schemes have been proposed, the first one uses active cooling (fig. 1.10) and the other uses passive cooling (fig. 1.11).

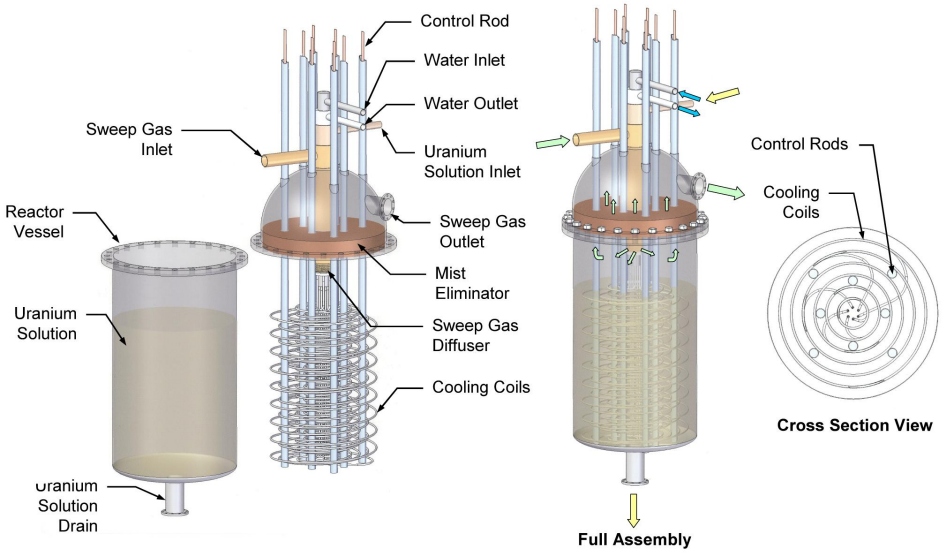

Figure 1.10: Diagram of the MIPR reactor vessel when using forced cooling as proposed by the Babcock & Wilcox Company. The diameter of the reactor vessel is 54.4 cm. The spirals are part of the cooling system.

As a first step, B&W did research[26] by irradiating a 500 mL capsule at the RA-6 facility in Bariloche, Argentina. The capsule contained an uranyl nitrate solution. The goal of the research was to show that ^{99}Mo can be produced safely from an uranyl nitrate solution. This was done as a part of the Proof-of-Principle required to get their licenses from the US Nuclear Regulatory Commission and the US Food and Drug Administration for operation a MIPR.

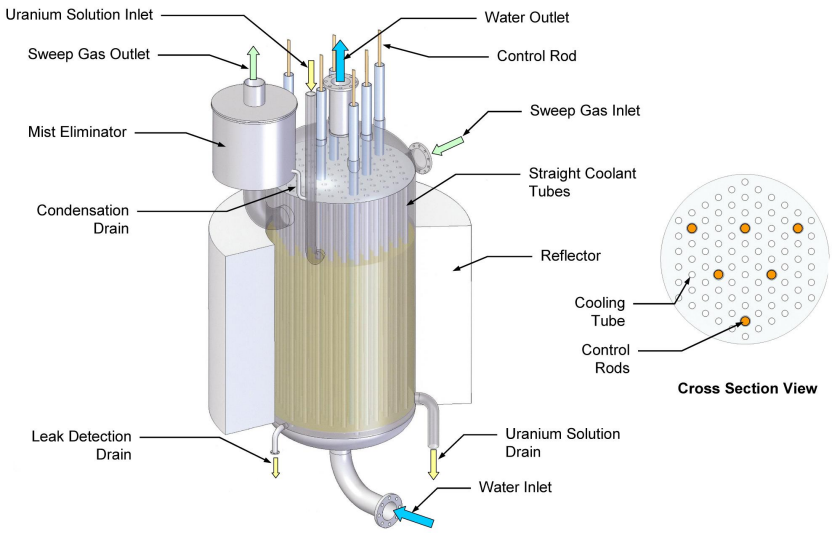

Figure 1.11: Diagram of the MIPR reactor vessel when using natural circulation cooling as designed by the Babcock & Wilcox Company. The diameter of the reactor vessel is 54.4 cm. The coolant flows from bottom to top.

An overview of all the different systems discussed in this chapter can be found in tab. 1.1. The conceptual designs are more detailedly specified in tab. 1.2.

Table 1.1: An overview of the different Aqueous Homogeneous research solution Reactors with their specifications.

System	**Developer**	**Years of operation**	**Fuel**	**Concentration**	**Enrichment**	**Size**	**^{99}Mo extraction method**	**Ref.**
SUPO	LANL, USA	1951-1974	Uranyl sulphate	$75\,\mathrm{g\,U\,L^{-1}}$	88.7 %	12.6 L spherical	n.a.	[7][13][27]
Argus	Kurchatov Institute, Russia	1989-	Uranyl sulphate	$88\,\mathrm{g\,U\,L^{-1}}$	90 %	20 L cylinder	Batch	[19][20]
Argus	Kurchatov Institute, Russia	1989-	Uranyl sulphate	$475\,\mathrm{g\,U\,L^{-1}}$	20 %	20 L cylinder	Batch	[19][20]
SR-RN	IPPE, Russia	Conceptual design	Uranyl sulphate	$94.4\,\mathrm{g\,U\,L^{-1}}$	90 %	20 L cylinder	Continuous	[21]
SHEBA II	LANL, USA	1993-	Uranyl nitrate	$190\,\mathrm{g\,U\,L^{-1}}$	20 %	80 L annular cylinder	n.a.	[13][14][15]
SHEBA II	LANL, USA	1993-	Uranyl fluoride	$1000\,\mathrm{g\,U\,L^{-1}}$	5 %	80 L annular cylinder	n.a.	[13][14][15]
TRACY	NUCEF, Japan	1995-	Uranyl nitrate	$380\,\mathrm{g\,U\,L^{-1}}$	10 %	117 L cylinder	n.a.	[16]
SILENE	CEA, France	1997-	Uranyl nitrate	$70\,\mathrm{g\,U\,L^{-1}}$	93 %	20 L annular cylinder	n.a.	[17]
MIPR	NPIC, China	Conceptual design	Uranyl nitrate	$50\,\mathrm{g\,U\,L^{-1}L}$	90 %	100 L cylinder	Batch	[22]
SAMOP	BATAN, Indonesia	Conceptual design	Uranyl nitrate	$300\,\mathrm{g\,U\,L^{-1}}$	20 %	5.6 L cylinder	Continuous	[24][23]
MIPR	The B&W Company, USA	Conceptual design	Uranyl nitrate	$125\,\mathrm{g\,U\,L^{-1}}$	19.75 %	142 L cylinder	Batch	[25]

Table 1.2: Detailed specification of the conceptual designs mentioned in tab. 1.1.

	SR-RN	**MIPR**	**SAMOP**	**MIPR**
Developer	IPPE, Russia	NPIC, China	BATAN, Indonesia	The B&W Company, USA
References	[21]	[22]	[24][23]	[25][28]
Fuel	Uranyl sulphate	Uranyl nitrate	Uranyl nitrate	Uranyl nitrate
Concentration	$94.4\,\mathrm{g\,U\,L^{-1}}$	$50\,\mathrm{g\,U\,L^{-1}}$	$300\,\mathrm{g\,U\,L^{-1}}$	$125\,\mathrm{g\,U\,L^{-1}}$
Enrichment	90 %	90 %	20 %	19.75 %
Size	20 L cylinder	100 L cylinder	5.6 L cylinder	142 L cylinder
^{99}Mo extraction method	Continuous	Batch	Continuous	Batch
Solution pH				1
Average thermal flux	0.59×10^{12} $\mathrm{n\,cm^{-2}\,s^{-1}}$	$\sim 10^{8}$ $\mathrm{n\,cm^{-2}\,s^{-1}}$	$1{\sim}2 \times 10^{12}$ $\mathrm{n\,cm^{-2}\,s^{-1}}$	
Radiolytic gas production		$50\,\mathrm{L\,s^{-1}}$		$1\,\mathrm{L\,s^{-1}}$
Solution Temperature	80 °C	70 °C		80 °C
Air pressure	0.89 atm	0.89 atm		0.92 atm
Production of ^{99}Mo	770 6-day Ci	500 Ci	300-480 mCi	1100 6-day Ci
Production cycle	1 week	3 days	3 days	1 week
Average power density	$1.5\,\mathrm{kW\,L^{-1}}$	$2{\sim}2.5\,\mathrm{kW\,L^{-1}}$		$1{\sim}2\,\mathrm{kW\,L^{-1}}$
Average radiolytic voids				2-4 %
Heat removal	Cooling coils, inlet 39 °C and outlet 74 °C with $4.2\,\mathrm{kg\,s^{-1}}$	Cooling coils, inlet 20 °C and outlet 40 °C with $2\,\mathrm{kg\,s^{-1}}$	Cooling tank, tank size: 2050 L	Cooling coils or natural convection

In order to put the production in context, the world demand for one week is 12 000 6-day Ci, see section 1.1.

1.5 Thesis goal and outline

Goal

The goal of this research is to investigate the feasibility of a small scale (i.e. 40 L) continuous filtering AHR for the production of ^{99}Mo. The chosen reactor size is smaller than the suggested designs by NPIC and B&W Company. In this way the impact of a downtime on the global production is reduced then when using larger reactors.

Outline

Chapter 2 describes the requirements which an AHR must meet. This includes the type of fuel, the gas management system, the reactor core design, ^{99}Mo extraction method and the cooling of the reactor.

In order to test the geometries, a thermo hydraulics code has been written. The model consist of an in-house developed Computational Fluid Dynamics code (HEAT) which is used in combination with a continuous energy Monte Carlo code called Serpent. These codes are described in chapter 3.

In chapter 4, the requirements set in chapter 2 and the model described in chapter 3 are used to investigate the safety of several geometries. The geometries are mainly assessed on their heat removal capability.

In chapter 5, the consumption of uranium is assessed based on the chosen geometry in chapter 4 and the reactivity feedback coefficient due to a change of temperature, xenon concentration and uranium concentration are calculated. Furthermore, a steady state calculation is done using the calculated feedback coefficients. In addition, the mass flow rate is varied to see the effect on the maximum power density, the total power and the ^{99}Mo outflow rate.

In chapter 6, a safety analysis is performed of the final chosen reactor. In total four type of transients will be investigated: a failure of the heat exchanger, a failure of the fission product filter, a change of the inlet uranium concentration and a reactivity insertion. Conclusions and further directions are discussed in chapter 7.

Chapter 2

Reactor design considerations

When designing an AHR, several aspects have to be addressed including the fuel used, the removal and recombination of radiolytic gases, the shape and size of the reactor, ^{99}Mo extraction and cooling.

2.1 Fuel compositions

In the AHRs mentioned in tab. 1.1, three type of fuel solutions of fuel are mentioned. These include uranyl sulphate, uranyl nitrate and uranyl fluoride. For each fuel the enrichment can be varied. Since the Non-Proliferation Treaty limits the enrichment for each fuel, only enrichments up 20 % are considered in this research[29].

2.1.1 Uranyl sulphate

Uranyl sulphate, UO_2SO_4 has widely been used in early solution reactors. Different properties of uranyl sulphate and especially those concerning with ^{99}Mo extraction have been listed below[30]:

+ Uranyl sulphate has a good radiation stability. The sulphate base does not disintegrate due to irradiation;
+ Only H_2 and O_2 are produced, which should be recombined back into water. In this way, the concentration of the uranium will not increase over time. If the concentration increases, so will the multiplication factor;
− Lower distribution coefficient than for uranyl nitrate. The distribution coefficient is the ratio of the ^{99}Mo concentration in the extraction filter and the ^{99}Mo concentration in the fuel. This is the reason that the recovery of molybdenum from uranyl sulphate solution is not as efficient as from an uranyl nitrate solution. The $(SO_4)^{2-}$ and $(HSO_4)^{-}$ bases interfere with the $(MoO_4)^{2-}$ base and therefore the ion exchange is less effective;
− Solubility of uranyl sulphate is low; the solubility in water at 25 °C is 275 g L^{-1} [31]. When the pH-level is lowered the solubility will increased.

2.1.2 Uranyl nitrate

The relevant properties[30] of uranyl nitrate fuel, $UO_2(NO_3)_2$, are:

+ Higher distribution coefficient for ^{99}Mo extraction than for uranyl sulphate, therefore a better recovery of molybdenum;
+ Good solubility of uranyl nitrate ($\sim$660 g L^{-1} [31]);
+ Viscosity of uranyl nitrate is lower than for uranyl sulphate, meaning less pumping is needed;
– Radiation stability is worse than for uranyl sulphate;
– Besides H_2 and O_2, N_2 and NO_x are also formed;
    - When NO_x gases are formed, the pH level will increase and the solubility decreases. Therefore the solution will no longer be fully dissolved and it will precipitate at the bottom.
    - This leads to a complex gas loop where the NO_x has to be removed or recombined. NO_x is flammable and should be handled with care;
– ^{14}C is formed through (n-p) reaction of ^{14}N, but only in small amounts. The half-life time of ^{14}C is approximatly 5730 years.

2.1.3 Uranyl fluoride

Uranyl fluoride (UO_2F_2) can also be used as fuel, but is not very common in an AHR. The combination of uranium with fluoride is more commonly used in molten salt reactors. The characteristics [32] of uranyl fluoride are:

+ the low neutron capture cross-section of fluorine, means less uranyl fluoride is needed to get the reactor critical;
– This fuel type is not often used in AHRs, see tab. 1.1. Uranyl fluoride is used in other solution reactors like the zero power reactor at Lewis Research Center (USA[33]), where highly enriched ^{235}U was used during the seventies;
– Hydrogen fluoride is produced, which can be found in both the liquid phase and the gas. In both phases it is very corrosive towards zirconium and titanium, but less corrosive towards stainless steel.

2.1.4 Criticality study for the different fuels and enrichments

The infinite multiplication factor, k_∞, has been calculated for different types of fuel using SCALE XSDRNDM. SCALE is a nuclear simulation program developed by Oak Ridge National Laboratory. XSDRNDM is used for finding k_∞ for a infinite homogeneous material. Fig. 2.1 shows the k_∞ for different fuels, concentration and enrichments. The uranium used in the simulation is LEU with different levels of enrichment, see fig. 2.1. The fuel has traces of ^{234}U present, which have been calculated using the method described in appendix A. The multiplication factors of the studied fuels are relatively close.

Of the solutions investigated uranyl nitrate has the lowest k_∞, which is expected since nitrate has a larger neutron absorption cross section. For higher concentrations of uranium, the ratio of uranium and water is lower. Because of the decrease of water also less moderation is done leading to a flattening of the k_∞. These obtained results are in close agreement with the calculations performed by the PINSTECH institute in Pakistan[34].

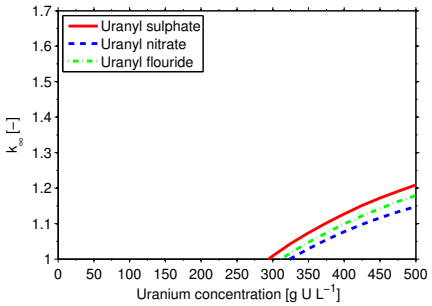

(a) For an enrichment of 5 %, uranyl sulphate has the highest multiplication factor due to fact that the base (i.e. sulphate) has an overall lower neutron absorption cross section.

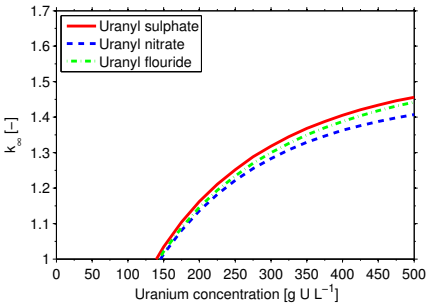

(b) For an enrichment of 10 % the same effect can be seen as in subfig. (a). For higher concentrations the ratio between uranium and water (the moderator) is higher. Therefore less moderation is done leading to a flattening of the curve.

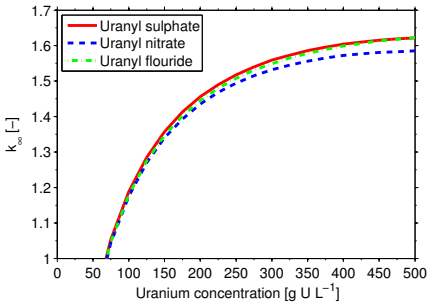

(c) For an enrichment of 20 % the effect of subfig. (b) is enhanced.

Figure 2.1: The infinite multiplication factor, k_∞, as a function of concentration for three solutions and three uranium enrichments.

2.1.5 The choice of the fuel

The choice of the level of enrichment is 20 %, this ensures that the concentration would not exceed the solubility.

The production of ^{99}Mo is the main goal of the reactor. Therefore the best fuel type is uranyl nitrate as ^{99}Mo is extracted more efficiently from uranyl nitrate than from uranyl sulphate. The fact that an uranyl nitrate gas management system is complexer outweighs the higher yield of ^{99}Mo. The low multiplication factor can be compensated by dissolving more uranyl nitrate in the AHR. By increasing the uranium concentration in the system, more uranium will be irradiated and therefore more ^{99}Mo will be produced. Uranyl fluoride will not be used as fuel sine this fuel type produces a hydrofluoric gas which is toxic and the experience with this fuel is limited.

Note that by looking at the overview of the conceptual designs of table 2, one can conclude that no overall preference exist for the type of fuel. However uranyl nitrate turns out performing better due to an higher yield.

2.2 Gas management system

A problem when using AHRs is the fact that radiolytic gases and fission products are produced. The radiolytic gases or radiolitic boiling is the effect of radiation splitting molecules into several components[18]. In all AHRs water will be split into hydrogen and oxygen gas:

$$2H_2O \overset{(n,\gamma)}{\rightarrow} 2H_2 + O_2. \tag{2.1}$$

These two gases should be recombined to ensure a constant fuel concentration. In order to recombine oxygen and hydrogen, two different methods can be used, namely a catalyst or a burner[32]. The catalyst should have a large surface and can be made for example of platinized alumina[11]. The flame recombiner is best described as an oversized Bunsen or Meeker burner enclosed in a water-jacketed cylinder[32]. This method can be risky due to the explosive character of the gas mixture.

When using uranyl nitrate as a fuel, NO_3 will be decomposed in nitrogen, oxygen and mono-nitrogen oxides:

$$NO_3 \overset{(n,\gamma)}{\rightarrow} \frac{\alpha}{2}N_2 + \left(\frac{3}{2}\alpha + \frac{(3-x)}{2}\beta\right)O_2 + \beta NO_x, \tag{2.2}$$

$$\alpha + \beta = 1. \tag{2.3}$$

The NO_x gases can either be recombined or disposed. When disposing NO_x, the nitrate should be replace with nitric acid to maintain a constant pH level.

The gases that are produced due to fission of uranium are krypton, xenon and iodine. These gases should be removed from the system, because of their high neutron absorption cross sections.

In this thesis only the effect of ^{135}Xe is accounted for. Furthermore the gas recombiner loop is not taken into consideration in this research.

2.3 Reactor core design

The core shape of the reactor does not depend on the type of fuel. A basic layout is depicted in fig. 2.2. Still, there are several things to keep in mind[30][35][36]:

- The height of the solution should be smaller than the diameter of the reactor. The produced gases will therefore have a shorter distance to travel to the surface, therefore minimizing the void fraction. The void fraction is the ratio between gas and liquid;
- The pressure of the air above the fuel should be below atmospheric pressure, otherwise gases can accumulate in the fluid;
- The maximum power density for future reactors is set to be $2.5\,\mathrm{kW\,L^{-1}}$, because experience with the SILENE reactor is that higher power densities lead to instabilities;
- The capacity of the recombination of H_2 and O_2 should be sufficient, otherwise the mixture can become explosive. Therefore the hydrogen concentration in the gas loop should be lower than 2 %;
- The inlet for the gas loop should be high enough above the water level to avoid liquid entering the gas loop;
- The pH-level should be below 3, otherwise uranyl can precipitate and accumulate at the bottom of the reactor vessel.

With these considerations the geometries of chapter 4 are designed.

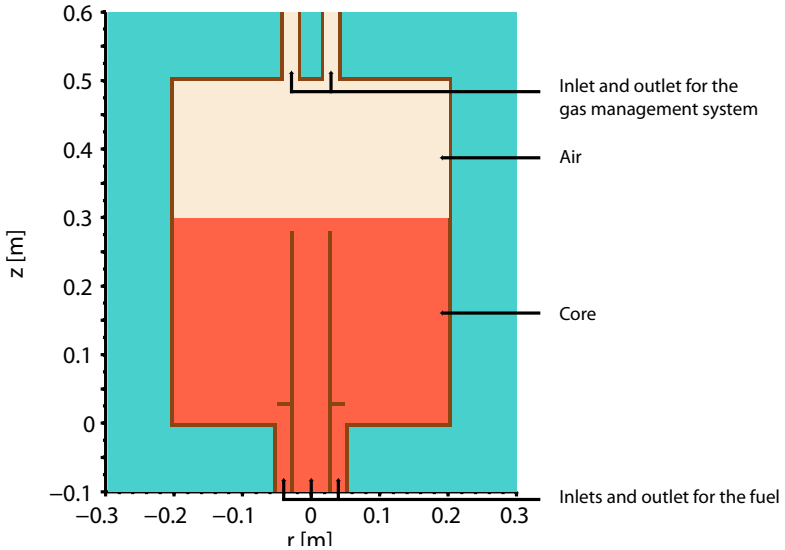

Figure 2.2: Basic layout of an AHR. Red indicates the fuel, brown indicates the structural material, beige indicates air and blue indicates the water reflector.

2.4 Molybdenum-99 extraction

The classic inorganic sorbent for ^{99}Mo recovery from acidic solutions is alumina, but Argonne National Laboratory also tested the Thermoxid sorbents (Isosorb and Radsorb) and the polyzirconium compound (PZC) sorbent[30]. All four were tested on efficient recovery of ^{99}Mo. The conclusion was that the Thermoxid sorbents were performing better for uranyl nitrate than for uranyl sulphate. The PZC could only be successful for uranyl nitrate. Generally ^{99}Mo is easier to extracted from uranyl nitrate than from uranyl sulphate.

The decision is made to use continuous filtering in stead of batch production, due to fact an higher yield of molybdenum-99[37]. The choice of the filter type will be left aside, since the focus of this research is the geometry inside the reactor vessel.

2.5 Cooling methods

A typical AHR has a total power of 50 kW, therefore cooling is needed. The cooling of a solution reactor vessel can be done both passively and actively[28].

Passive cooling

The reactor vessel can be cooled passively by fins on the outside or by coiling coils through the core. The benefit of using passive cooling is that it is reliable. The drawback is that the reactor power is limited and a large pool is required, because the temperature difference within the AHR is roughly 50 K the natural convection is not strong enough. Cooling coils throughout the reactor increases the heat transfer, but a larger surface area is exposed to acidity of the fuel.

Active cooling

In active cooling, the coolant is pumped though the coils. The cooling coils can be placed inside the reactor vessel. The drawback is that boiling will still occur between the coils, when the power density is too high. The advection is not strong enough to spread out the heat fast enough through the system. Another way of active cooling is using the fuel as a coolant. This method is also applied in a molten salt reactor. The fluid will be cooled externally by a heat exchanger.

Since the extraction of ^{99}Mo is continuously, the fluid is already pumped around through the system. Therefore its convenient to place the heat exchanger in the same loop.

Chapter 3

Modeling of the system

The geometries that will be considered in chapter 4 are solved using a coupled scheme. The scheme consist of a neutronics part to calculate the heat production due to fission and criticality and a Computational Fluid Dynamics code for the flow and temperature distribution. In this chapter is explained both codes are separately and also the coupling between the two codes.

3.1 Neutronics

The neutronics is calculated using the program Serpent[38] which is still under development.The code is still extended by VTT Technical Research Centre of Finland under the supervision of Jaakko Leppänen. Serpent is a continuous energy Monte Carlo code which is capable of using parallel processing. The Monte Carlo simulates large numbers of neutrons in order to get the different characteristics of the system like the neutron flux. The benefits of using Serpent are that the output files are written in Matlab format, making them easy to couple with other codes. Furthermore how to write the input needed for Serpent is well documented. With diffusion codes one has to worry about how to collapse the different cross sections, this is not necessary with a Monte Carlo. The drawback when using a Monte Carlo based code is time consuming for finding an effective multiplication factor with relative error below 0.0001. The cross section library ENDF/B-VII is used for the nuclear data. Furthermore, Serpent has the capability to calculate the fuel burnup. This thesis uses Serpent version 2.1.12.

3.1.1 Serpent input

The fuel inside the reactor vessel will be split up to 20×40 spatial elements, the spatial dependence of the geometry is given in fig.3.1. The size of the spatial element is a compromise between spatial dependence and the fact that the Monte Carlo particles will stop at the interface to sample again. This is due to the fact that each spatial element has a different cross sections. The concentration of ^{99}Mo and ^{135}Xe will be volume averaged, see subsection 3.3.3. The temperature cannot be set spatially due to memory errors on the cluster, because Serpent will try to store too many continuous energy cross sections libraries and subsequently crashes. Therefore the average fuel temperature will be used uniformly for the whole system.

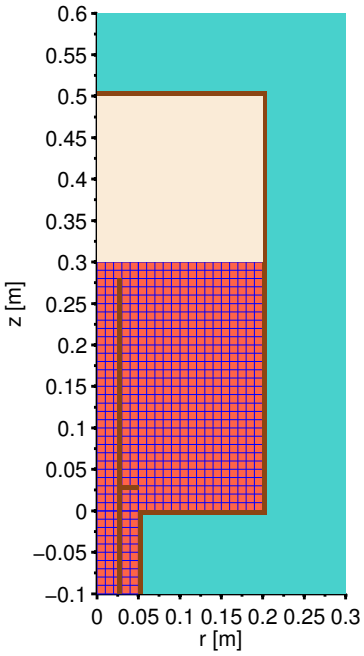

Figure 3.1: The spatial elements used in Serpent using the *Bulge* geometry (see chapter 4) as an example. Red indicates the fuel, brown indicates the structural material, beige indicates air and blue indicates the water reflector.

3.1.2 Serpent output

Serpent will solve the system in three dimensions for the power density, isotope production density and the effective multiplication factor k_{eff}. The power density and k_{eff} are standard features of Serpent. The isotope production density is calculated from the total fission rate (ENDF reaction mode MT 18) multiplied by the uranium concentration and is defined as:

$$S(\vec{r}) = \frac{1}{V} \int_V \int_E C_{^{235}U}(\vec{r})\, \Sigma_{f_{tot}}(\vec{r}, E)\, \phi(\vec{r}, E)\, dE d\vec{r}, \tag{3.1}$$

where V is the volume of a detector cell, E is energy of the neutron, $C_{^{235}U}$ is the ^{235}U concentration, $\Sigma_{f_{tot}}$ is the total fission cross section (MT 18), ϕ is the neutron flux and $\vec{r}$ is the spatial dependence.

3.2 Fluid Dynamics

Computational Fluid Dynamics (CFD) is done with the help HEAT, which is an in-house two dimensional CFD code based on books of Versteeg[39] and Patanka[40]. As a natural choice, the CFD code of the AHR is based on the CFD code for a molten salt fast reactor[41]. The molten salt reactor HEAT was capable of solving the Reynolds Average Navier-Stokes equation. These parts of the code have been preserved and extended, for the case when the flow is predominantly turbulent. The flow in this thesis are all predominantly laminar, therefore this has not been used. The highest Reynolds number will be found in the outflow tube which is approximately 3000.

3.2.1 Modeled equations

The flow of the fluid can be described by the Navier-Stokes equation:

$$\rho\left(\frac{\partial\vec{v}}{\partial t}+\vec{v}\cdot\vec{\nabla}\vec{v}\right)=\frac{1}{2}\vec{\nabla}\cdot\left\{\mu\left(\vec{\nabla}\vec{v}+\left(\vec{\nabla}\vec{v}\right)^{T}\right)\right\}-\vec{\nabla}p+\vec{F_b}, \tag{3.2}$$

where ρ is the density, $\vec{v}$ is the velocity vector, p is the pressure field, μ is the dynamic viscosity and $\vec{F_b}$ is the gravity force. The terms from left to right are the local rate of change, convection, diffusion, pressure force and the body force. In HEAT a first order approximation is made for the gravity force induce by including differences in temperature of fluid. The gravitational force is described as:

$$\vec{F_b}=\rho(T)\vec{g}\approx\rho\vec{g}\left[1-\beta_{ref}\left(T-T_{ref}\right)\right], \tag{3.3}$$

where β_{ref} is the thermal expansion coefficient and T_{ref} the corresponding reference temperature. Since the temperature change in the system will be small, the Boussinesq approximation for buoyancy is used. This means that the temperature has only an effect on the gravitational term. The energy balance is given by:

$$\rho C_p\left(\frac{\partial T}{\partial t}+\vec{v}\cdot\vec{\nabla}T\right)=\vec{\nabla}\cdot\left(\lambda\vec{\nabla}T\right)+P, \tag{3.4}$$

here C_p is the specific heat capacity, λ is the thermal conductivity and P is the power. The terms from left to right are the local rate of change, convection, diffusion and production term.

Two isotopes are being tracked namely ^{99}Mo and ^{135}Xe. ^{99}Mo is the medical isotope of interest and ^{135}Xe is a significant neutron absorber. The assumption is made that all gas phase fission products stay inside the liquid, so the concentration of these isotopes will be higher than in reality. The balances for both isotopes are:

$$\frac{\partial C_{^{99}\mathrm{Mo}}}{\partial t}+\vec{v}\cdot\vec{\nabla}C_{^{99}\mathrm{Mo}} = \vec{\nabla}\cdot\left(D\vec{\nabla}C_{^{99}\mathrm{Mo}}\right)+\gamma_{^{99}\mathrm{Mo}}S-\frac{1}{\tau_{^{99}\mathrm{Mo}}}C_{^{99}\mathrm{Mo}}, \tag{3.5}$$

$$\frac{\partial C_{^{135}\mathrm{Xe}}}{\partial t}+\vec{v}\cdot\vec{\nabla}C_{^{135}\mathrm{Xe}} = \vec{\nabla}\cdot\left(D\vec{\nabla}C_{^{135}\mathrm{Xe}}\right)+\gamma_{^{135}\mathrm{Xe}}S-\frac{1}{\tau_{^{135}\mathrm{Xe}}}C_{^{135}\mathrm{Xe}}, \tag{3.6}$$

where C_i is the concentration of the isotopes, D is the diffusion coefficient for particles, γ_i is the cumulative fission yield, S is the isotope production density (see eq. 3.1) and τ_i is the decay constant. The terms in eq. 3.5 and eq. 3.6 are from left to right the local rate of change, convection, diffusion, production and decay term.

The last equation is the concentration of the uranium in the fuel. In chapter 6, the effect of a chaningin uranium concentration is taken into account. The uranium balance is given by:

$$\frac{\partial C_U}{\partial t}+\vec{v}\cdot\vec{\nabla}C_U=\vec{\nabla}\cdot\left(D\vec{\nabla}C_U\right), \tag{3.7}$$

where C_U is the concentration of uranium. The terms from left to right are the local rate of change, convection and diffusion term. The loss of uranium due to fission is negligible and therefore not modeled. The change of concentration also has an effect on the density of the fluid due to high mass of the uranium isotopes. In appendix A, the method is described for calculating the density of the fluid.

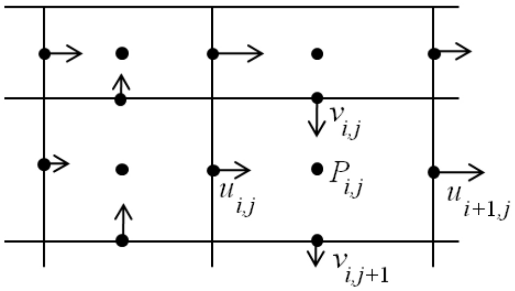

Figure 3.2: Schematics of a staggered grid. Scalar quantities are located in the center of the volume elements. The velocity components are located at the cell boundaries[41].

3.2.2 Numerical method

HEAT solves the equation in a staggered grid. This means that the velocity vector components are located at the boundaries of the volume elements, whereas the scalar quantities like pressure and temperature are given at the center of the volume elements. See fig. 3.2 for an illustration[41]. In order to maintain mass conservation, a pressure correction method is used namely the SIMPLE routine. The threshold is set to 10^{-4} Pa which is strict enough due to the fact that typical pressures drops of the system are around 1 to 10 Pa. An implicit scheme is used to solve each equation.

Several assumptions have to be set in order to make HEAT work. The effect of the irradiation on the uranyl nitrate solution is assumed negligible, since the total power levels of an AHR are small. The outflow in all geometries described in chapter 4 are turbulent, but the remainder of the system is laminar. Since this part is more important, HEAT will run without the turbulence model. The last assumption made is the fact that gas will not escape from the fluid to the air above the liquid. The gas concentration will be overestimated, but the concentration is rather small due to the low power density.

3.2.3 Boundary conditions

Inlet(s)

Inlet velocity is defined as a fully developed laminar flow in an annulus, which has been scaled to have a specific mass flow rate. The ^{99}Mo and ^{135}Xe concentrations are set zero at the inlet, because the assumption is made that all fission products are removed from the fuel. During the steady state calculations, the uranium inflow concentration equals the initial uranium concentration. In chapter 6 transients will be investigated, there the inlet concentration varies over time depending on the cause.

Outlet

At the outflow of the fluid all parameters like velocity and temperature have a zero gradient in the flow direction. In other words the outflow pipe has such a length that the flow is fully developed. The pressure is set to be zero at the outflow.

Walls

The walls inside the reactor vessel have a no-slip boundary condition, the interface between the fluid and air has a free-slip condition. The temperature boundary have a zero gradient

at $Z = 0.3\,\text{m}$ and $R = 0.2\,\text{m}$. The temperature at the "wall" at the bottom of the system is set at 30 °C. In fig.3.3 an overview of these conditions are depicted.

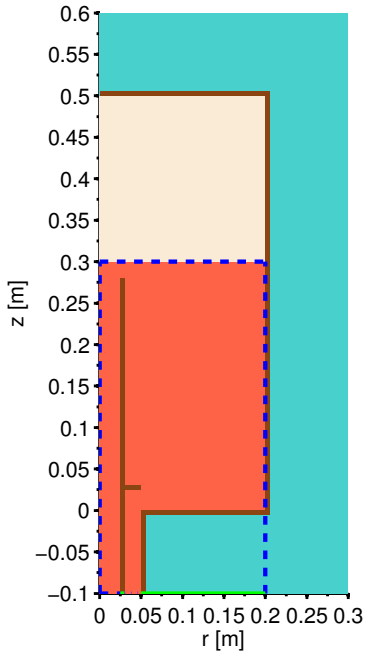

Figure 3.3: Temperature boundaries used in HEAT, where the *Bulge* geometry has been used as example. The blue dashed line indicates an insulted wall, the green line is the fixed temperature boundary and the purple dotted line is the inlet temperature. Furthermore, red indicate the fuel, brown indicates the structural material, beige indicates air and blue indicates the water reflector.

3.2.4 Mesh refinement

In order to get a reliable result from HEAT, the mesh should be fine enough. Four geometries will be tested in chapter 4, see fig.3.4 for an overview. The mesh of the geometries named *bulge* and *vertical plates* have a mesh size of $(1 \times 1)\,\text{mm}$, i.e. a grid size of 200×400. The name of the geometry refers to the lay-out of the structural material in the reactor vessel. The *bulge* geometry uses a small bulge to direct the flow and the *vertical plates* geometry uses vertical plates to direct the flow. The chosen meshes are fine enough, since they are even finer than then those discussed in the next paragraph.

For the *horizontal plates* and *bulkheads* geometries a homogeneous grid size is not possible due to the fact that the structural material thickness inside the vessel is 0.5 mm. The *horizontal plates* geometry uses horizontal plates to direct the flow and the *bulkheads* geometry uses vertical walls in collaboration with four inlets to direct the flow, this geometry is the only geometry with multiple inlets. The solver will have difficulties in solving 320 000 nodes, therefore a non-uniform grid is chosen. The chosen grid size varies from 0.5 to 5 mm. In order to know whether the chosen mesh is fine enough to get a reliable result, the mesh is refined even more with a factor of two. The mesh refinements can be seen in fig. 3.5 and fig. 3.6. As can be seen, the ^{99}Mo concentration profiles hardly change, therefore the chosen meshes are fine enough and will be used in chapter 4.

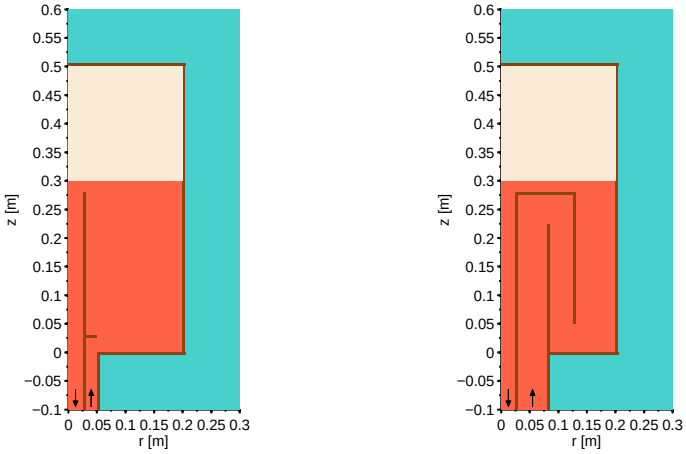

(a) The *Bulge* geometry

(b) The *Vertical plates* geometry

(c) The *Horizontal plates* geometry

(d) The *Bulkheads* geometry

Figure 3.4: An overview of the different geometries used in chapter 4. Red indicates the fuel, brown indicates the structural material, beige indicates air and blue indicates the water reflector.

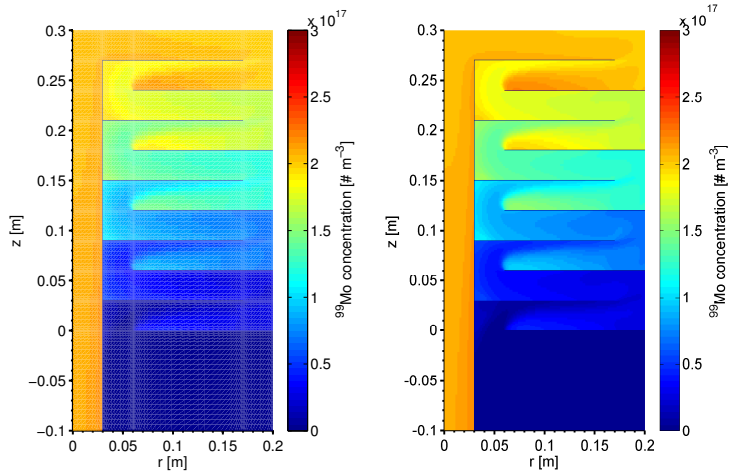

(a) HEAT solution for a grid size of 71×143 nodes.

(b) HEAT solution for a grid size of 142×286 nodes.

Figure 3.5: The result of the mesh refinement of *horizontal plates* geometry for the ^{99}Mo concentration.

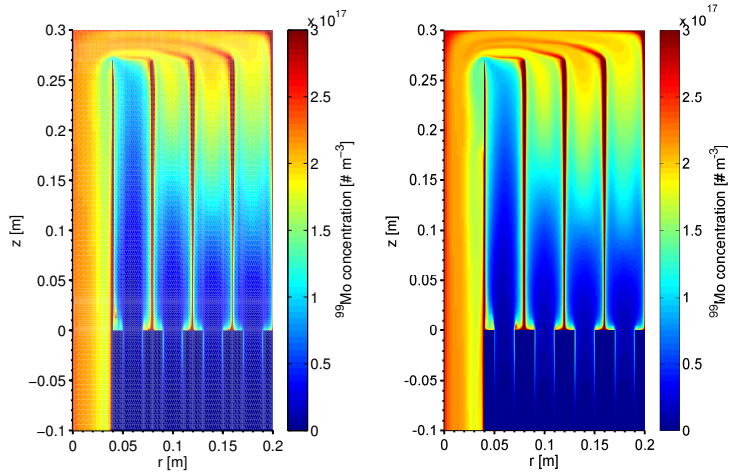

(a) HEAT solution for a grid size of 138×123 nodes.

(b) HEAT solution for a grid size of 276×246 nodes.

Figure 3.6: The result of the mesh refinement of *bulkheads* geometry for the ^{99}Mo concentration.

3.3 Coupling of Serpent with HEAT

3.3.1 Steady state calculations

In order to a find steady state solution of an AHR, the scheme of fig. 3.7 is used. At the beginning a power guess is made. HEAT and Serpent are used sequentially until the reactivity and the temperature field are both converged. HEAT is stopped when the maximum change in the system is below $0.01\,\mathrm{K\,s^{-1}}$, Serpent is tuned to have a relative error of the multiplication factor of around 10^{-4}. Depending on the effective multiplication factor, the power is lowered or raised. This process is repeated until the effective multiplication factor within the error margin.

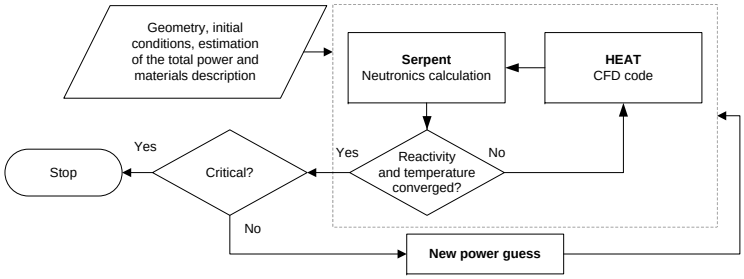

Figure 3.7: The calculation scheme for finding the steady state solution. The scheme consist of two loops, the first one runs HEAT and Serpent sequentially until both temperature and reactivity are converged. The secondary loop checks whether the system is critical and adjusts the total power if needed.

3.3.2 Transient calculations

In chapter 6 transient analysis is performed to check the safety of an AHR. In order to save a lot of computational time, Serpent is replaced with point kinetics, as Serpent run takes up to four hours to calculate the multiplication factor with an uncertainty of 10^{-4}. The point kinetics equations represent a very simplified model, for instance the convection of precursors are not modeled. The model will provide an indication of the effects certain transients can have on the system. The point kinetics equation are defined as[42]:

$$\frac{\mathrm{d}p}{\mathrm{d}t} = \frac{\rho(t)-\beta}{\Lambda}p + \sum_f \lambda_f c_f, \tag{3.8}$$

$$\frac{\mathrm{d}c_f}{\mathrm{d}t} = -\lambda_f c_f + \frac{\beta_f}{\Lambda}p, \tag{3.9}$$

where p is the power amplitude function, $\rho(t)$ is the reactivity, β is the effective delayed neutron fraction, Λ is the generation time, λ_f is the precursor decay constant, c_f is the precursor density, β_f is the precursor delayed neutron fraction and f is an indicator of a delayed group. In total six delayed groups will be used. The reactivity will be defined as:

$$\rho(t) = \rho(\bar{T}(t)) + \rho(\bar{C}_{^{135}\mathrm{Xe}}(t)) + \rho(\bar{C}_U(t)) + \rho_{ext}, \tag{3.10}$$

where $\rho(\bar{T})$ is the reactivity as a function of the average temperature, $\rho(\bar{C}_{^{135}\mathrm{Xe}})$ is the reactivity as a function of the average ^{135}Xe concentration, $\rho(\bar{C}_U)$ is the reactivity as a

function of the average uranium concentration and ρ_{ext} is the external reactivity insertion. The three dependent reactivities will be calculated in section 5.2.

The generation time, delayed neutron fraction and precursor decay constants are calculated by Serpent. The assumption is made that these values will not change significantly over time.

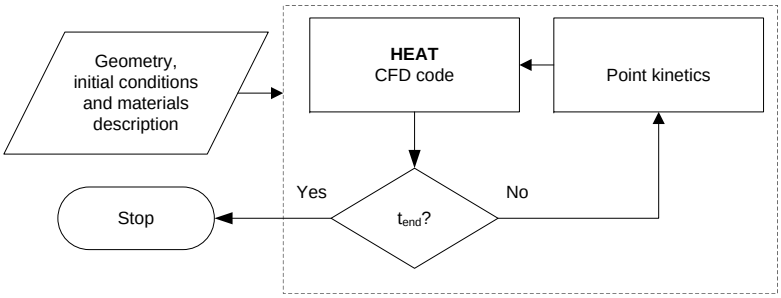

Figure 3.8: The calculation scheme for a transient calculation. The neutronics is given by a point kinetics model. The time step used in point kinetics is always 1 µs, since this is thw time of the precursors. However, the time step in HEAT can depend on the transient applied.

3.3.3 Exchange of data

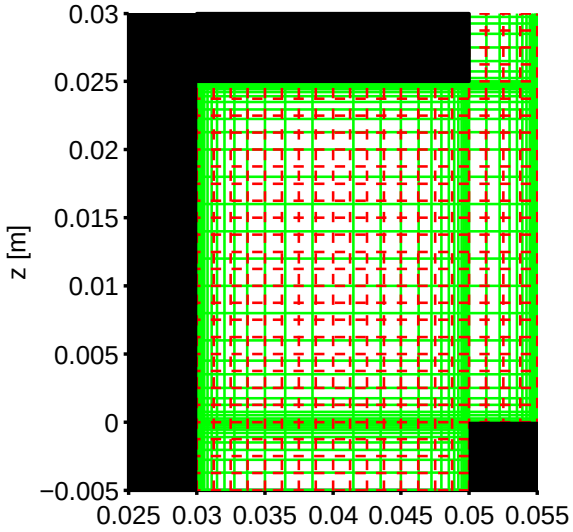

Figure 3.9: A close-up of the mesh at the entrance of the *bulge* geometry, see fig. 4.1. The structural material is colored black, the green cells are used by HEAT and the red (dashed) cells are used by Serpent

In order to exchange data between Serpent and HEAT a mesh transformation is required. The HEAT mesh sometimes overlaps multiple Serpent cells or vice versa. An example can be seen in fig. 3.9. The transformation is done by volume averaging and is defined by the following equation:

$$C^{\mathrm{H}} = \frac{\sum_i V_i C_i^{\mathrm{S}}}{\sum_i V_i}, \tag{3.11}$$

where C_i^{S} is the power density or isotope production density in a Serpent cell and C_i^{H} is the volume averaged value in the HEAT cell. The term V_i is the volume of the Serpent cell that overlaps the corresponding HEAT cell. Therefore the summation of all volumes V_i should be equal to the volume of the corresponding HEAT cell. Despite of a non uniform HEAT mesh, it is still structured. To make the mesh transformation easier to perform, the transformation is split into a R-component and a Z-component. The definition of the transformation factor of the Z-component is given by:

$$F_z(i,j) = \frac{\Delta z(i)^{\mathrm{S}}}{\Delta z(j)^{\mathrm{H}}}, \tag{3.12}$$

where $\Delta z(j)^{\mathrm{H}}$ is the height of the HEAT cell and $\Delta z(i)^{\mathrm{S}}$ is the height of the Serpent cell which is inside the HEAT cell. The definition of the R-component is given by:

$$F_r(i,j) = \frac{\left(r(i)_{out}^2 - r(i)_{in}^2\right)^{\mathrm{S}}}{\left(r(j)_{out}^2 - r(j)_{in}^2\right)^{\mathrm{H}}}. \tag{3.13}$$

For the R-component of the transformation factor, one should account for the fact that cylindrical coordinates are used. Where $r(i)_{in}$ is distance of the inner wall to the center axis and $r(i)_{out}$ for the outer wall. Therefore $\left(r_{out}^2 - r_{in}^2\right)$ is used as a fraction, but the rest of the calculation is done in a similar way as for the Z-component. This means that

$\left(r(i)^2_{out} - r(i)^2_{in}\right)^{\mathrm{S}}$ still has to lie inside the HEAT cell. With these two components eq. 3.11 becomes:

$$C^{\mathrm{H}} = F_r^T C^{\mathrm{S}} F_z. \tag{3.14}$$

A similar method is also used for the transformation of the temperature from HEAT to Serpent. An example of this transformation can be seen in fig. 3.10. To check whether the

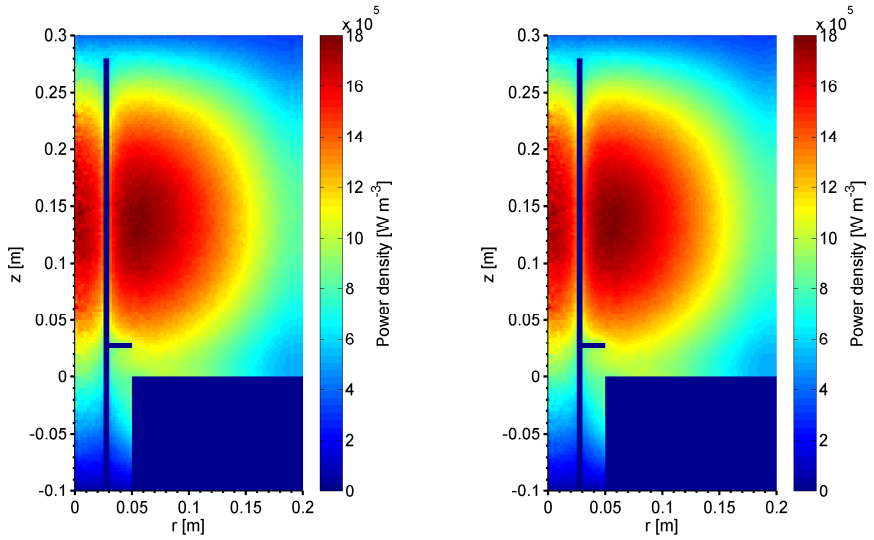

(a) Serpent output

(b) HEAT input

Figure 3.10: The result of a mesh transformation from Serpent to HEAT for the power density, using the volume averaging method. The values indicate the deposition of the fission energy.

transformation from Serpent to HEAT is correct, the total fission energy depositions in both systems are calculated and they should be the same. The transformation as shown in fig 3.10 passed this test.

3.4 Material properties

Since no extensive database of material properties of uranyl nitrate exist, water properties are used whenever the properties of uranyl nitrate are not available. An overview of these materials can be found in table 3.1. The material properties of the surrounding material can be found in tab. 3.2 and for the isotopes ^{99}Mo and ^{135}Xe the properties can be found in table 3.3. The density of the fluid is calculated using the theory described in appendix A.

Table 3.1: An overview of the relevant material properties of uranyl nitrate.

	value	**water property used?**	**ref.**
Diffusion coefficient	$1 \times 10^{-9}\,\mathrm{m^2\,s^{-1}}$	yes	[43]
Dynamic viscosity	$0.546 \times 10^{-3}\,\mathrm{Pa\,s}$	yes	[43]
Specific heat capacity	$2.7211 \times 10^{3}\,\mathrm{J\,K^{-1}\,kg^{-1}}$	no	[44]
Thermal conductivity	$0.665\,\mathrm{W\,m^{-1}\,K^{-1}}$	yes	[43]
Thermal expansion coefficient	$5.9653 \times 10^{-3}\,\mathrm{K^{-1}}$	yes	[43]
Reference temperature of thermal expansion coefficient	$346.15\,\mathrm{K}$	yes	[43]

Table 3.2: An overview of the relevant material properties of the surrounding material.

	value	**Material**	**ref.**
Density	$1 \times 10^{3}\,\mathrm{kg\,m^{-3}}$	water	[43]
Specific heat capacity	$4.1816 \times 10^{3}\,\mathrm{J\,K^{-1}\,kg^{-1}}$	water	[43]
Thermal conductivity	$0.665\,\mathrm{W\,m^{-1}\,K^{-1}}$	water	[43]
Density	$7.999 \times 10^{3}\,\mathrm{kg\,m^{-3}}$	SS304	[45]
Specific heat capacity	$4.1875 \times 10^{3}\,\mathrm{J\,K^{-1}\,kg^{-1}}$	SS304	[45]
Thermal conductivity	$0.51\,\mathrm{W\,m^{-1}\,K^{-1}}$	SS304	[45]
Density	$1.2\,\mathrm{kg\,m^{-3}}$	air	[43]
Specific heat capacity	$1.009 \times 10^{3}\,\mathrm{J\,K^{-1}\,kg^{-1}}$	air	[43]
Thermal conductivity	$3.3 \times 10^{-2}\,\mathrm{W\,m^{-1}\,K^{-1}}$	air	[43]

Table 3.3: An overview of the relevant material properties of ^{99}Mo and ^{135}Xe.

	value	**Material**	**ref.**
Cumulative Fission Yield	6.138 69 %	^{99}Mo	[46]
Half-life time	65.94 hours	^{99}Mo	[46]
Cumulative Fission Yield	6.523 01 %	^{135}Xe	[47]
Half-life time	9.14 hours	^{135}Xe	[47]

Chapter 4

Reactor design calculations

A large number of geometries were tested to see whether they are suitable for molybdenum-99 (^{99}Mo) production, namely:

- *Bulge* geometry,
- *Vertical plates* geometry,
- *Horizontal plates* geometry,
- *Bulkheads* geometry, which includes multiple inlets.

The main criteria is the removal of heat, so that the maximum temperature in the system remains below the boiling point of water, because the water vapor will create instabilities.

In the following sections, the main types of geometries are discussed including several minor variations on these geometries. The geometries *Bulge* and *Vertical plates* where tested when the CFD code did not include a model for the xenon and uranium concentrations. The last two geometries were tested using the model described in chapter 3.

4.1 *Bulge* Geometry

The first geometry which was tested is a simple cylindrical vessel where a bulge was added to enhance mixing of the fuel. This geometry is depicted in fig. 4.1. The outflow and inflow of the fuel is located at the bottom. The outflow is through the inner tube and the inflow through the outer annulus. The inflow is $0.4\,\mathrm{kg\,s^{-1}}$ with $300\,\mathrm{g\,U\,L^{-1}}$ and the total power was set to 37 kW. The corresponding power density profile can be seen in fig. 4.2.

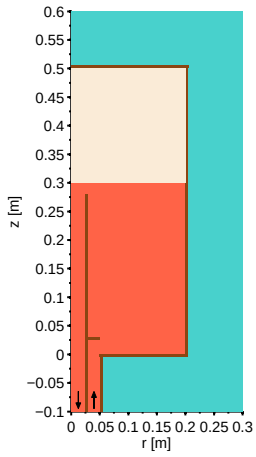

Figure 4.1: Cross section of the *bulge* geometry. Red indicates the fuel, brown indicates the structural material, beige indicates air and blue indicates the water reflector.

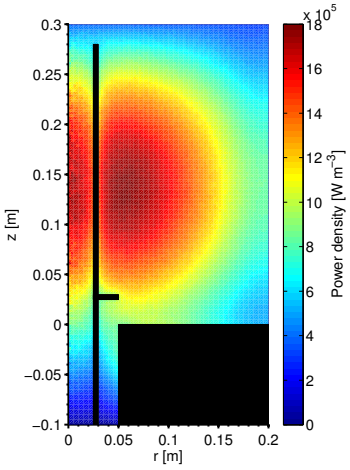

Figure 4.2: Power density profile of the *bulge* geometry.

Fig. 4.3 shows that buoyancy and thermal diffusion are not capable of spreading sufficiently. The vortex seen in fig. 4.4 is stronger than the buoyancy term and thermal diffusion, hence a hot spot is created.

The width of the bulge has been varied between 2 cm and 15 cm. The change of bulge width has an effect on size and location of the vortex position and the hot spot, but the hot spot did not disappear. In order to remove the hot spot above the bulge, a small gap between the bulge and the outflow tube was created. This modification had the desired result, however it did not have an effect on the size and location on main hot spot.

The conclusion is that this geometry is not suitable for the AHR and that the flow should be guided through the vessel to avoid hot spots.

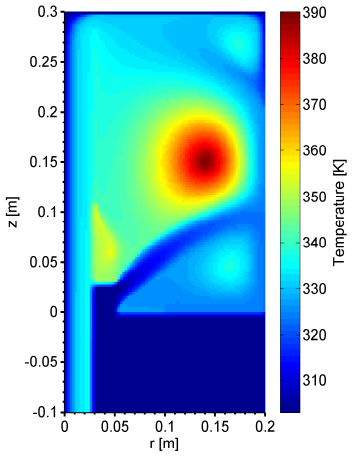

Figure 4.3: Temperature profile of the *bulge* geometry, the hot spot is clearly visible as a red spot. It is at the same location as the vortex shown in fig. 4.4.

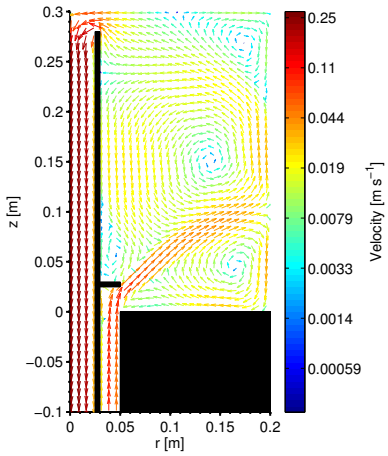

Figure 4.4: Velocity vector plot of the *bulge* geometry. Next to the big vortex, a vortex can be seen above the bulge and below the cold "jet" of fuel.

4.2 *Vertical plates* Geometry

In order to improve the heat removal by the fluid flow, a new geometry was tested. This geometry is depicted in fig. 4.5. In this setting, the flow is directed to stay close to the center of the core. Whenever the top is reached, the flow is directed downwards. At the bottom, the flow is directed upwards again and the fuel flows along an air-feul interface to the outlet. The geometry is similar to the design of a high performance light water reactor[48]. The idea behind this geometry is that the "cold" fuel will first pass a zone where a lot of heat is produced. In this way the maximum temperature inside the core will not exceed 100 °C. The uranium concentration and the mass flow rate are the same as for the *bulge* geometry.

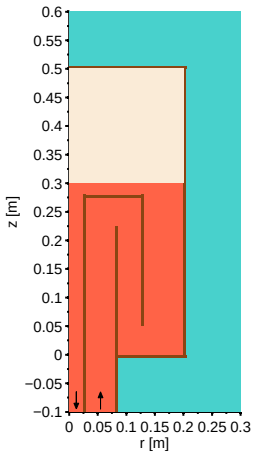

Figure 4.5: Cross section of the *vertical plates* geometry. Red indicates the fuel, brown indicates the structural material, beige indicates air and blue indicates the water reflector.

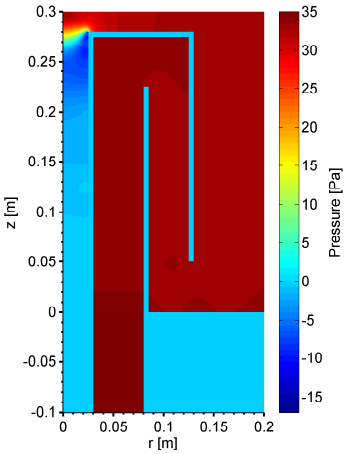

Figure 4.6: Pressure profile of the *vertical plates* geometry. A relative large pressure drop can be seen in the outflow tube. This is due to fact that the fluid is accelerated due to smaller cross-sectional area.

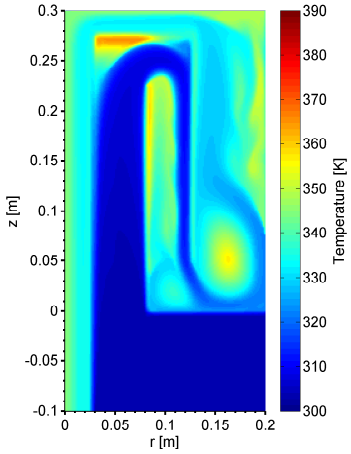

Figure 4.7: Temperature profile of the *vertical plates* geometry. Two hot spots can be seen; one at the top of the inflow tube due to a lack of fluid motion and one at the bottom which is due to vortices created when the fluid moves upwards for the second time.

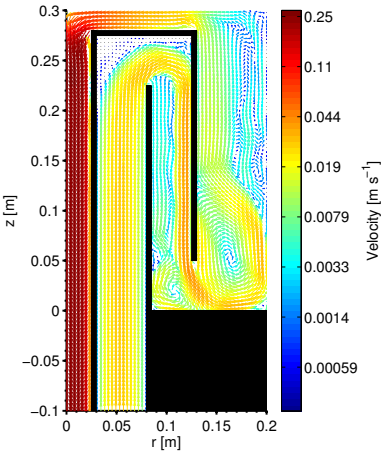

Figure 4.8: Velocity vector plot of the *vertical plates* geometry. When the flow is directed downwards for the first time, the buoyancy is strong enough to counteract the flow.

For this geometry, the total power is identical to the power of the *bulge* geometry. The power density looks similar as the one depicted in fig. 4.2. As can be seen in fig. 4.8, no large vortex is present in the system, but smaller vortices and a dead zone can be seen. The maximum temperature for this geometry is just below the boiling point of water (365 K), which can be a problem because the water vapor cannot escape due to the design of this specific geometry. The reason why a lower maximum temperature is desired the better mixing of the fuel and therefore a better spreading of the heat. Due to the temperature difference in the fuel, the buoyancy dominates the flow pattern near the hot spot, which can be seen in figs. 4.7 and 4.8. The main pressure drop, as depicted in fig. 4.6, is produced by the accelerating of the fluid decrease of surface area.

The buoyancy effect in the downward flow can be suppressed by reducing the width of the channel, but this will increase the size of the vortex at the bottom. The same is true for making the vertical gaps smaller; this will reduce the temperature, but the vortices will be stronger.

Although this geometry can be used, it is not ideal. The possible accumulation of gas at the dead zone can be dangerous. Therefore, in the next tested geometries gas should only flow upwards or horizontal expect for the outflow tube.

4.3 *Horizontal plates* Geometry

The next step was to check whether horizontal plates are better than vertical plates. In this way no gas can get trapped in the system and the heat is better spread along the flow direction. The number of horizontal plates and the distance between the two plates have been varied. The geometry that is best capable of removing heat is shown in fig. 4.9. It consists of nine horizontal plates that are evenly distributed over the height of the core. The flow is always directed upwards, and so gas pockets will not occur. The high number of horizontal plates are there to ensure that the vortex at each turning point is suppressed enough and no hot spots are formed.

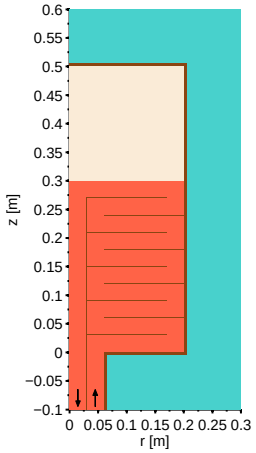

Figure 4.9: Cross section of the *horizontal plates* geometry. Red indicates the fuel, brown indicates the structural material, beige indicates air and blue indicates the water reflector.

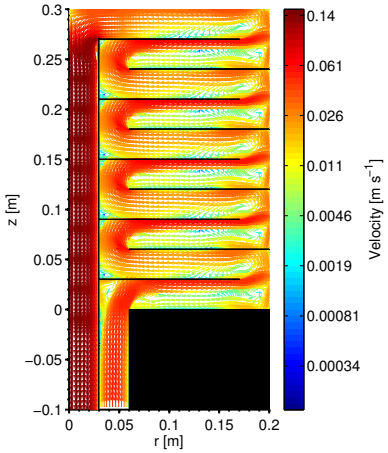

Figure 4.10: Velocity vector plot of the *horizontal plates* geometry. There are still vortices present in the system, but they do not create significant hot spots.

The uranium concentration is $307\,\mathrm{g\,U\,L^{-1}}$ and the total amount of uranium in the system is 11.8 kg. The inlet mass flow rate is still $0.4\,\mathrm{kg\,s^{-1}}$. The velocity vector plot is depicted in fig. 4.10. In contrast with previous velocity plots no large vortices are present. When the fluid flows between two plates from left to right, a large back flow at the bottom can be seen. The effect of back flows are visible in the temperature profile (fig. 4.12) and the concentrations plots (fig. 4.15 and fig. 4.16), where the temperature and the concentration are higher than the main flow at the top.

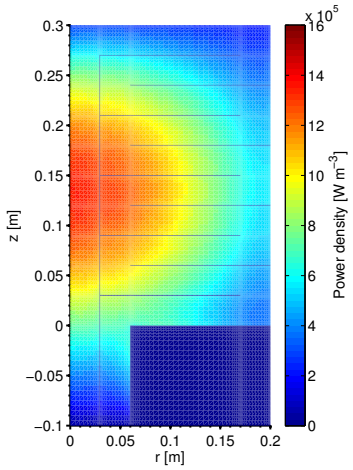

Figure 4.11: Power density profile of the *horizontal plates* geometry.

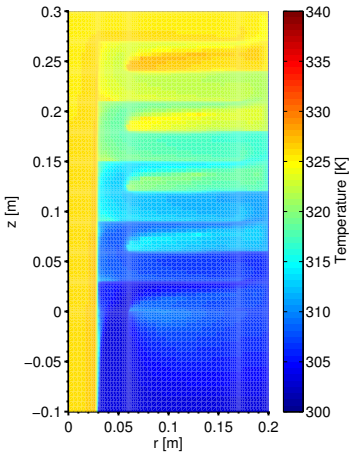

Figure 4.12: Temperature profile of the *horizontal plates* geometry. The temperature is slowly increasing when it flows through the system.

The power profile is shown in fig. 4.11. The steady state total power is 25.25 kW, with a maximum power density of $1.37\,\mathrm{kW\,L^{-1}}$, which is lower than the maximum value of $2.5\,\mathrm{kW\,L^{-1}}$ as stated in chapter 2. The temperature profile is depicted in fig. 4.12, where one can see that the maximum temperature is 327 K and the outflow temperature is 325 K, which is 22 K higher than the inlet temperature.

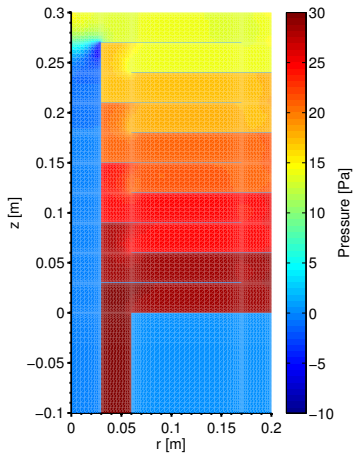

Figure 4.13: Pressure profile of the *horizontal plates* geometry.

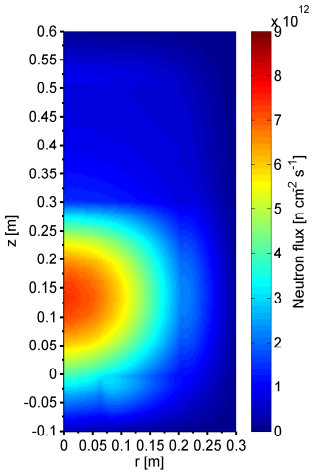

Figure 4.14: Total flux profile of the *horizontal plates* geometry. Note, the volume around the reactor core is also included in this figure.

The large number of horizontal plates increase the friction force on the fluid. In order to compensate for this effect, a larger pressure drop of 30.1 Pa is required, see fig. 4.13, to pump the fluid through the the system. This is the largest pressure drop of all four geometries investigated. The total flux of the system is depicted in fig. 4.14 and it can be seen that the maximum neutron flux is $7.46 \times 10^{12}\,\mathrm{n\,cm^{-2}\,s^{-1}}$. The outer structural material of the reactor vessel can be seen in the total flux profile. Air is a poor moderator and therefore the neutron flux is much lower than in the water reflector.

The ^{135}Xe and ^{99}Mo concentration profiles are depicted in fig. 4.15 and fig. 4.16. The concentration profiles of ^{135}Xe and ^{99}Mo are slightly different due to different cumulative fission yields. The maximum concentration of ^{135}Xe is $1.93 \times 10^{17}\,\#\,\mathrm{m^{-3}}$ and $1.82 \times 10^{17}\,\#\,\mathrm{m^{-3}}$ for ^{99}Mo. The outlet concentration of ^{99}Mo is $1.74 \times 10^{17}\,\#\,\mathrm{m^{-3}}$. If the AHR has operated for one day, the production will be 29.6 6-day Ci or 0.548 mg. The weekly production would be 207 6-day Ci, which is 1.72 % of the world demand.

The conclusion is that this geometry can be used as a method to spread out the heat, but the horizontal plates may be an obstacle when gas bubbles are present in the system. In other words, the bubbles can still be trapped in the system. Despite of the relative small reactor size, the production of ^{99}Mo is significant compared for its size.

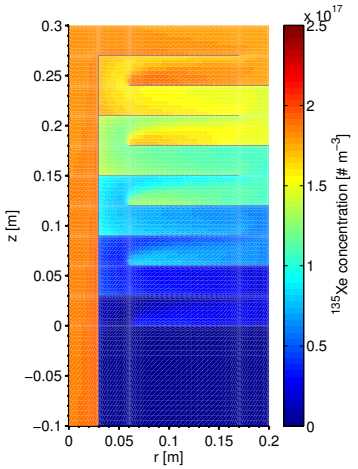

Figure 4.15: ^{135}Xe concentration profile of the *horizontal plates* geometry.

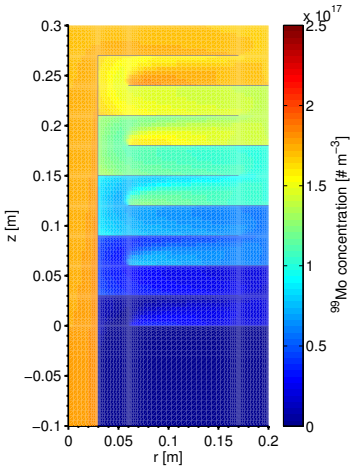

Figure 4.16: ^{99}Mo concentration profile of the *horizontal plates* geometry.

4.4 *Bulkheads* Geometry

As can be seen in the previous section, the horizontal plates are spreading the heat properly, but the geometry can be optimized even further. For this geometry, the mass flow rate of $0.4\,\mathrm{kg\,s^{-1}}$ is still used, but the uranium concentration is lowered to $248\,\mathrm{g\,U\,L^{-1}}$. The total amount of uranium is 10.9 kg, which is almost the same amount as used for the *horizontal plates* geometry. As seen in fig. 4.17, the geometry has four inlets instead of one and less structural material is needed to direct the flow. By using four inlets an upward flow can be created. This can be seen in fig. 4.18.

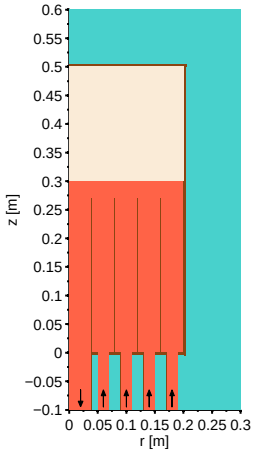

Figure 4.17: Cross section of the *bulkheads* geometry. Red indicates the fuel, brown indicates the structural material, beige indicates air and blue indicates the water reflector.

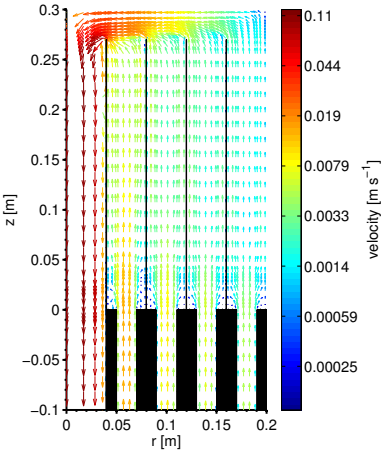

Figure 4.18: Velocity vector plot of the *bulkheads* geometry. This geometry does not show any large vortices.

At first, the idea was to have a velocity profile which is constant in the radial direction. With this distribution, each annulus needed the same time to reach the top of the reactor. This distribution was obtained by weighing the inlet mass flow rate by:

$$w_i = \frac{A_i}{\sum_i A_i}, \tag{4.1}$$

where A_i is the lateral surface of the inlet. This leads to a situation where the inlets will

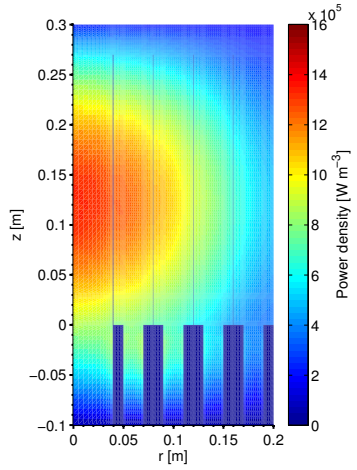

Figure 4.19: Power density profile of the *bulkheads* geometry. At the inlets fission is also occurring, leading to heat dissipation in the fuel.

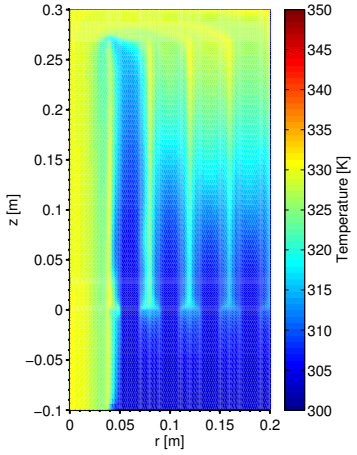

Figure 4.20: Temperature profile of the *bulkheads* geometry. The system does not have any hot spots.

have a significant difference in temperature at the top of the system. The total power in the inner annulus is lower than in the outer annulus, therefore the inner annulus is heated up more. Therefore, at the top of reactor layers are formed with each having a different temperature.

A more uniform temperature field is desirable for safety reasons, therefore the choice is made that the mass flow rate should be evenly distributed. The result is that the temperature profile is more uniform, which can be seen in fig. 4.20. The outflow temperature is 327 K, which is 24 K higher than the inflow temperature. Fig. 4.19 shows the power density distribution for the system, where the total power of the system is 27 kW. The effective multiplication factor (k_{eff}) of this system is 1.000 17 with an uncertainty of 5×10^{-5}.

When comparing the pressure profile of the *bulkheads* with the *horizontal plates*, a much lower pressure drop over the system of 6.5 Pa can be seen. This is due to the larger diameter of the outlet pipe and the shorter travel path of the fluid. The total flux has a maximum of $7.68 \times 10^{12}\,\mathrm{n\,cm^{-2}\,s^{-1}}$.

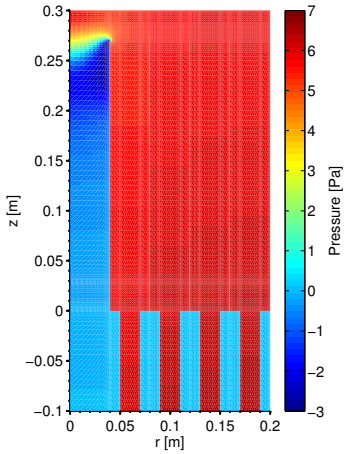

Figure 4.21: Pressure profile of the *bulkheads* geometry. This geometry has a smaller pressure drop as that of *horizontal plates* geometry, see fig. 4.13.

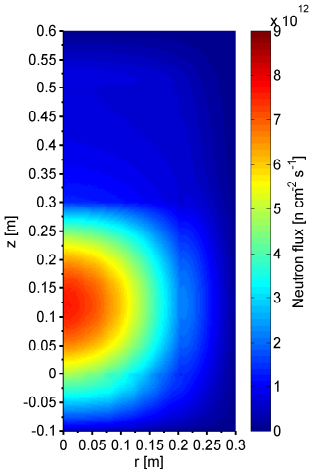

Figure 4.22: Total flux profile of the *bulkheads* geometry. The neutron flux in air is very low due to poor moderator capacitance of air.

In fig. 4.24 the ^{99}Mo concentration profile has been depicted. The outflow concentration is $1.88 \times 10^{17}\,\#\,\mathrm{m}^{-3}$. Since the cumulative fission yields are almost identical, the concentration profile of ^{135}Xe is similar to the concentration profile of ^{99}Mo, see fig.4.23. Near the bulkheads and at the upper right corner the concentration is up to five times

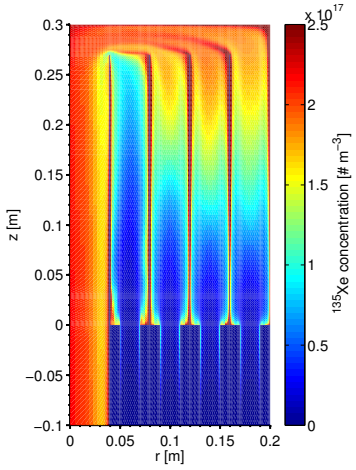

Figure 4.23: ^{135}Xe concentration profile of the *bulkheads* geometry.

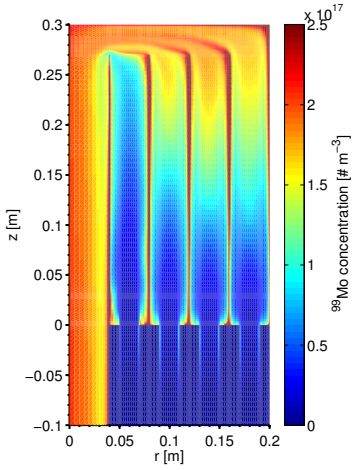

Figure 4.24: ^{99}Mo concentration profile of the *bulkheads* geometry.

higher than the outflow concentration. This is due to the low velocity and poor diffusion of the uranyl in water (i.e. no turbulent mixing). The highest concentration of ^{135}Xe is $9.86 \times 10^{17}\,\#\,\mathrm{m}^{-3}$ and $9.25 \times 10^{17}\,\#\,\mathrm{m}^{-3}$ for ^{99}Mo.

When the AHR will run for 24 hours, the total amount of ^{99}Mo produced equals 0.588 mg or 31.8 6-day Ci. This leads to a weekly production of 223 6-day Ci, which is roughly 1.8 % of the weekly world demand.

Chapter 5

Characteristics of the *Bulkheads* geometry

5.1 Burnup calculation

Using Serpent, a burnup calculation is done to calculate the uranium consumption. The reactor is run for two years, using the steady state solution of chapter 4.4 as the initial condition. The spatial dependence of the xenon and molybdenum concentrations will be neglected and replaced by an average value for the entire system. Only the average uranium concentration is important, because the circulation of the fuel leads to a homogeneous concentration in the reactor. The result of this calculation can be seen in fig. 5.1. The total

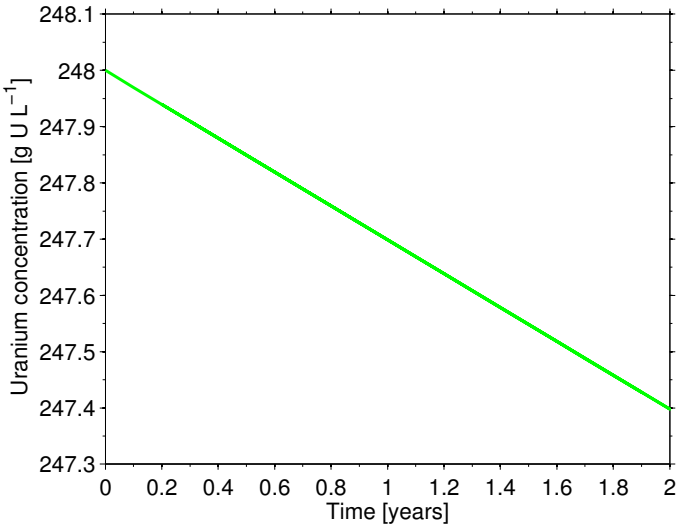

Figure 5.1: The concentration of uranium as a function of time. The uranium consumption is relative small due to the small power used of the AHR.

amount of uranium consumption is $6\,\mathrm{g\,year^{-1}}$, after when running the reactor non-stop. This implies that the assumption made in section 3.2.2 that the change in uranium concentration over time is marginal and can be considered as constant, is acceptable.

5.2 Reactivity feedback coefficients

In this section the reactivity feedback coefficients of the temperature, xenon concentration and uranium concentration are calculated, using the steady state results of section 4.4. Each reactivity coefficient has been calculated by alternating the value of the parameter. The reactivities were calculated using Serpent.

5.2.1 Temperature

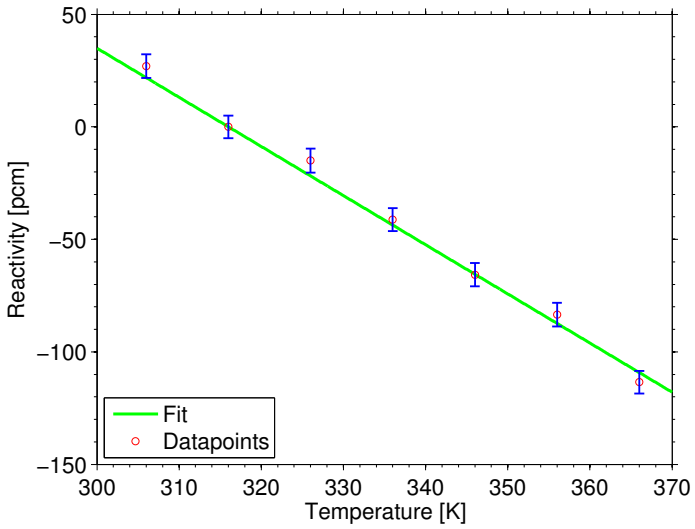

Figure 5.2: The reactivity as a function of the temperature, with a statistical uncertainty of 5 pcm.

The feedback is given by Doppler broadening, a widening of the resonance peaks in the absorption cross sections of the uranium isotopes. The feedback is approximated by a straight line:

$$\rho(\bar{T}(t)) = \alpha \left(\bar{T}(t) - T_{\text{ref}}\right), \tag{5.1}$$

where $\bar{T}(t)$ is the average fuel temperature as a function of time, T_{ref} is the reference average fuel temperature (316 K) and α is the temperature feedback coefficient ($-2.814\,\text{pcm}\,\text{K}^{-1}$). A reactivity feedback calculation as a function of the uranium concentration was performed with XSDRNDM and a temperature feedback coefficient of $-3.8\,\text{pcm}\,\text{K}^{-1}$ was found for $248\,\text{g}\,\text{U}\,\text{L}^{-1}$, see fig. 5.3. These values (Serpent and XSDRNDM) are much lower compared with the values reported in literature for the temperature feedback coefficient other AHRs. The HRT has a temperature feedback coefficient of $-100\,\text{pcm}\,\text{K}^{-1}$ to $-200\,\text{pcm}\,\text{K}^{-1}$[49]. The other reactor at ORNL, the aqueous homogeneous research reactor (HRR) has a temperature feedback coefficient of $-90\,\text{pcm}\,\text{K}^{-1}$ at 298 K[32].

A recent publication[50] of Imperial College London shows a temperature feedback coefficient of $-19.2\,\text{pcm}\,\text{K}^{-1}$ for their system. The fuel used is 20 % enriched uranyl nitrate and the concentration is $145\,\text{g}\,\text{U}\,\text{L}^{-1}$. The main difference between this research and that of Imperial is that Imperial also varied the density of the fuel as a function of the temperature.

The values reported by ORNL uses different concentrations, fuel types and enrichments. Therefore the feedback coefficient provided by Serpent will be used as the temperature feedback coefficient. The coefficient calculated with the help of SCALE is in close agreement with the one obtained using Serpent.

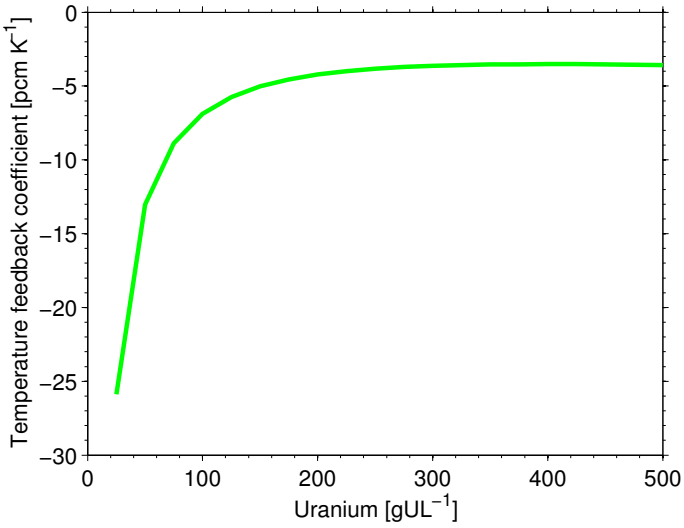

Figure 5.3: The temperature feedback coefficient as a function of the uranium concentration. The results were calculated with SCALE XSDRN in order to verify the temperature feedback coefficient calculated with Serpent. Both coefficients for a concentration of $248\,\mathrm{g\,U\,L^{-1}}$ have a similar order of magnitude.

5.2.2 Xenon concentration

The reactivity as a function of the relative xenon concentration is depicted in fig. 5.4. The feedback of the ^{135}Xe concentration is much weaker than that of the temperature. An increase of the ^{135}Xe concentration will lead to more absorption of the neutron, since ^{135}Xe is a known neutron absorber. An higher order fit is used to have a better fit for the feedback coefficient:

$$\begin{aligned}\rho(\bar{C}_{^{135}\mathrm{Xe}}(t)) \quad = \quad & \alpha\left(\bar{C}_{^{135}\mathrm{Xe}}(t) - C_{^{135}\mathrm{Xe}_{\mathrm{ref}}}\right)^3 + \\ & \beta\left(\bar{C}_{^{135}\mathrm{Xe}}(t) - C_{^{135}\mathrm{Xe}_{\mathrm{ref}}}\right)^2 - \\ & \gamma\left(\bar{C}_{^{135}\mathrm{Xe}}(t) - C_{^{135}\mathrm{Xe}_{\mathrm{ref}}}\right),\end{aligned} \tag{5.2}$$

where $\bar{C}_{^{135}\mathrm{Xe}}(t)$ is the average xenon concentration as function of time, $C_{^{135}\mathrm{Xe}_{\mathrm{ref}}}$ is the average reference concentration and α, β and γ are fitting parameters, their estimated values are:

α	$5.761 \times 10^{-60}\ \frac{\mathrm{pcm}}{\#^3\,\mathrm{m}^{-9}}$
β	$1.007 \times 10^{-41}\ \frac{\mathrm{pcm}}{\#^2\,\mathrm{m}^{-6}}$
γ	$-2.596 \times 10^{-18}\ \frac{\mathrm{pcm}}{\#\,\mathrm{m}^{-3}}$
$C_{^{135}\mathrm{Xe}_{\mathrm{ref}}}$	$1.12 \times 10^{17}\,\#\,\mathrm{m}^{-3}$

The feedback coefficient at average reference concentration equals $-2.596 \times 10^{-18}\ \frac{\mathrm{pcm}}{\#\,\mathrm{m}^{-3}}$, which will give a lower feedback than temperature. During the burnup calculation the maximum xenon concentration in the system is $5.66 \times 10^{19}\,\#\,\mathrm{m}^{-3}$, which is 505 times larger than the reference concentration.

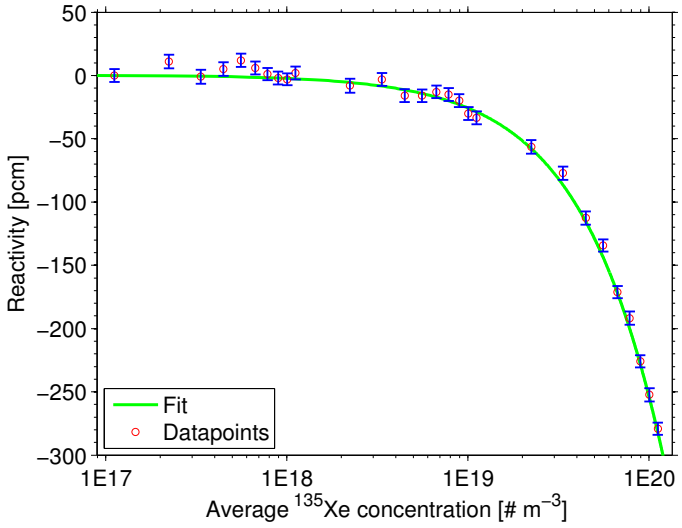

Figure 5.4: The reactivity as a function of the change of the xenon concentration. Each calculated data point has a statistical uncertainty of 5 pcm.

5.2.3 Uranium concentration

The reactivity feedback of the uranium concentration is depicted in fig. 5.5. The change in uranium concentration has a large effect on the reactivity. This effect is expected because during the steady state calculation of the chapter 4.4, the system was sensitive for the uranium concentration. The uranium concentration feedback is approximated by a quadratical polynomial:

$$\begin{aligned} \rho(\bar{C}_U(t)) &= \alpha \left(\bar{C}_U(t) - C_{U_{\text{ref}}}\right)^2 + \\ &\quad \beta \left(\bar{C}_U(t) - C_{U_{\text{ref}}}\right), \end{aligned} \tag{5.3}$$

where $\bar{C}_U$ is the average uranium concentration in the system, $C_{U_{\text{ref}}}$ is the reference uranium concentration and α and β are fitting parameters. Their values are:

α	$-0.377 \frac{\text{pcm}}{\text{g}^2\,\text{U}^2\,\text{L}^{-2}}$
β	$65.96 \frac{\text{pcm}}{\text{g U L}^{-1}}$
$C_{U_{\text{ref}}}$	$248\,\text{g U L}^{-1}$

The feedback coefficient of the uranium concentration around the reference concentration is $65.96 \frac{\text{pcm}}{\text{g U L}^{-1}}$. This positive feedback is much stronger than the temperature or xenon concentration feedback coefficient. Each geometry has a very specific uranium concentration and it is the main parameter that determines if the system is critical.

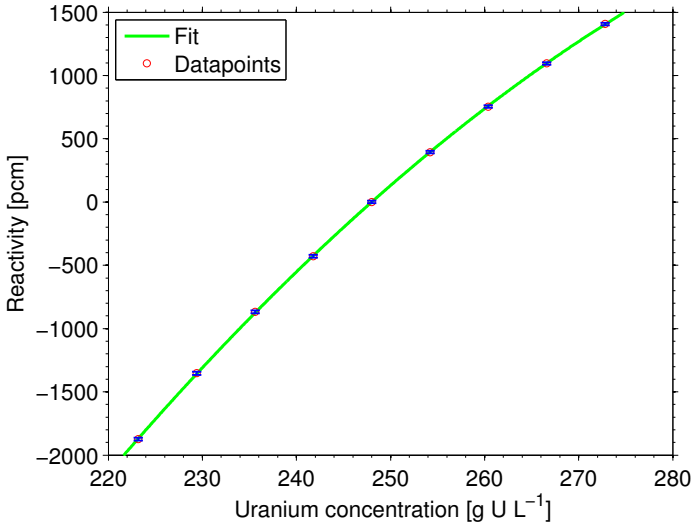

Figure 5.5: The reactivity as a function of change of the uranium concentration. The feedback is much stronger than for the temperature and xenon concentration. The errorbars shown in the plot above are relative small, the average uncertainty is around 5 pcm for each points.

5.2.4 Verification of the reactivity polynomial fits

The polynomials of the previous section all depend on a single parameter (i.e. temperature, xenon concentration or uranium concentration). In this section a check is performed to see whether these parameters depend on each other. First, two of the three parameters are changed and subsequently all parameters are changed. The temperature is increased by 30 K, the uranium concentration is increased with 15 g U L^{-1} and the xenon concentration is increased with a factor of hundred. The result is shown in tab. 5.1. The polynomial fits are

Table 5.1: Validation of the polynomial fits. The polynomial fits are within two statistical uncertainties as provide by Serpent.

Temperature	**Uranium concentration**	**Xenon concentration**	**Polynomial fits**	**Serpent**
+30 K	+ 15 g U L^{-1}	1x	839 pcm	834 pcm ± 5 pcm
+30 K	+ 0 g U L^{-1}	100x	−94 pcm	−92 pcm ± 5 pcm
+0 K	+ 15 g U L^{-1}	100x	876 pcm	871 pcm ± 5 pcm
+30 K	+ 15 g U L^{-1}	100x	810 pcm	804 pcm ± 5 pcm

close to the results obtained using Serpent. Therefore the polynomial fits of the previous section will be used.

5.2.5 Point kinetics parameters

During the steady state calculation of section 4.4, Serpent also calculated values needed to do point kinetics with eqs. 3.8 and 3.9. The generation time is 6.1662×10^{-5} s, the precursor decay constant and precursor delayed neutron fractions are given in tab. 5.2. These parameters are used first for finding a steady state solution in the next section and for the transients calculations preformed in chapter 6. The sum of the precursor delayed neutron fraction or β equals 764.7 pcm.

Table 5.2: The group constants of the point kinetics.

Group	**Precursor decay constant** [s^{-1}]	**Precursor delayed neutron fraction** [–]
1	$1.249\,06 \times 10^{-2}$	$2.462\,19 \times 10^{-4}$
2	$3.181\,55 \times 10^{-2}$	$1.275\,17 \times 10^{-3}$
3	$1.094\,14 \times 10^{-1}$	$1.240\,50 \times 10^{-3}$
4	$3.171\,76 \times 10^{-1}$	$3.490\,95 \times 10^{-3}$
5	1.353 51	$1.030\,46 \times 10^{-3}$
6	8.650 19	$3.637\,75 \times 10^{-4}$

5.3 The effect of the mass flow rate

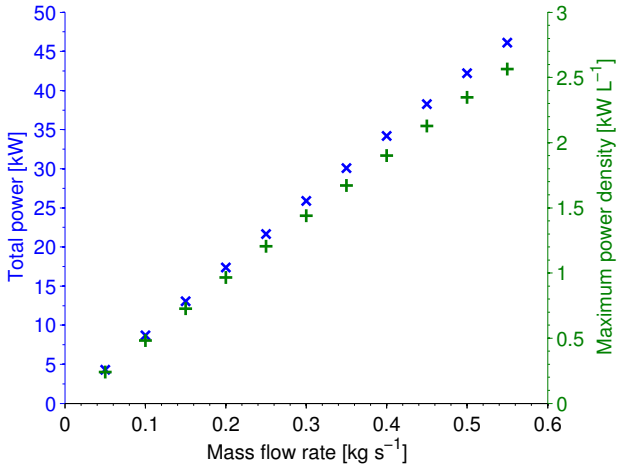

Figure 5.6: The total power(×) and the maximum power density(+) as a function of the mass flow rate. The power increases linear with the mass flow rate, since the total power divided by the mass flow rate is constant. This is also the reason that the temperature profile and xenon concentration profile roughly are the same for each mass flow rate.

Until know, the calculations have been performed with the same mass flow rate, namely $0.4\,\mathrm{kg\,s^{-1}}$. In this section the mass flow rate is varied between $0.05\,\mathrm{kg\,s^{-1}}$ and $0.55\,\mathrm{kg\,s^{-1}}$. The geometry of section 4.4 is still super critical with a multiplication factor of 1.000 17 ($0.4\,\mathrm{kg\,s^{-1}}$). Using the feedback mechanism of the previous section, the actual steady state is calculated. In fig. 5.6, the total power and the maximum

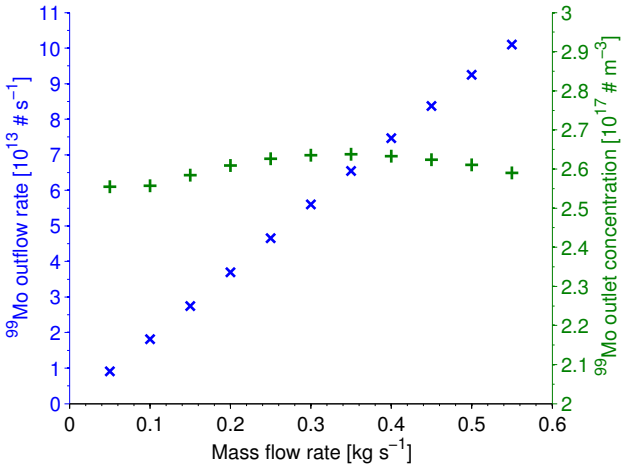

Figure 5.7: The total power(+) and the maximum power density(×) as a function of the mass flow rate. The ^{99}Mo concentration is constant, due to the same effective radiation for every mass flow rate. For higher mass flow rates the system time will be shorter, increasing the outflow rate of ^{99}Mo.

power density are depicted. Both parameters are linear with the mass flow rate. The mass flow rate of $0.55\,\mathrm{kg\,s^{-1}}$ has a maximum power density above the threshold set in chapter 2.3. The optimum mass flow rate is therefore approximately $0.50\,\mathrm{kg\,s^{-1}}$ and is chosen to be the new mass flow rate in the remainder of the this thesis.

As can be seen in fig. 5.7, the outlet concentration of ^{99}Mo does not depend on the mass flow rate. This is due to the fact that the residence time is inversely related with the mass flow rate and the production rate is linear with mass flow rate, therefore the outlet concentration stays constant. The outlet concentration stays constant in respect to the mass flow rate, since the irritation is the same. Therefore the outflow rate of ^{99}Mo is linear with the mass flow rate.

Properties of the steady state solution of a $0.5\,\mathrm{kg\,s^{-1}}$ mass flow rate

Due to the increase of the mass flow rate, the values and figures given in section 4.4 have been changed. The overall shape of the parameters remains the same, but their amplitudes increases (see fig. 5.8).

The total power for the mass flow rate is 42.2 kW, with a maximum power density of $2.35\,\mathrm{kW\,L^{-1}}$. The pressure drop over the system increases from 6.5 Pa to 10.2 Pa, which is still a relative small pressure drop. The maximum temperature of the system is 344 K and the outflow temperature equals 337 K. The maximum total neutron flux is $1.20 \times 10^{13}\,\mathrm{n\,cm^{-2}\,s^{-1}}$. The outflow ^{99}Mo concentration is raised from $1.88 \times 10^{17}\,\#\,\mathrm{m^{-3}}$ to $2.61 \times 10^{17}\,\#\,\mathrm{m^{-3}}$. The outflow ^{99}Mo concentration $1.88 \times 10^{17}\,\#\,\mathrm{m^{-3}}$ is calculated during the steady state calculation in chapter 4.4, here the total power is under estimated since the k_{eff} is 1.000 17. This leads to a weekly ^{99}Mo production of 309 6-day Ci, which is 86 6-day Ci more than the old situation.

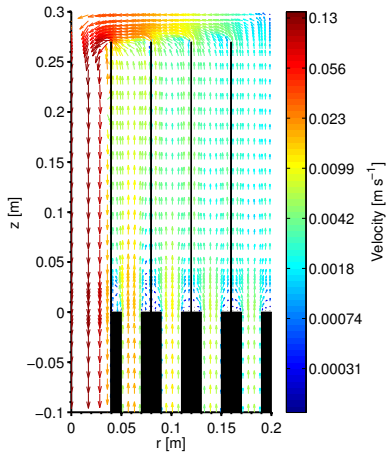

(a) Velocity vector plot

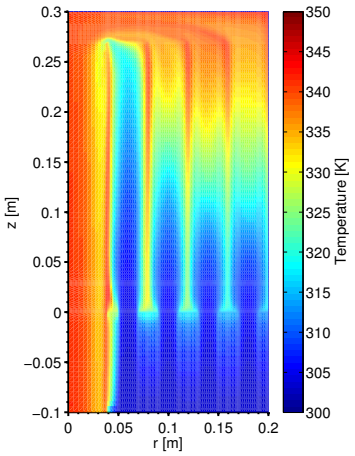

(b) Temperature profile

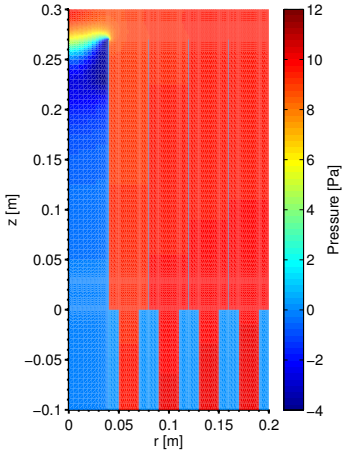

(c) Pressure profile

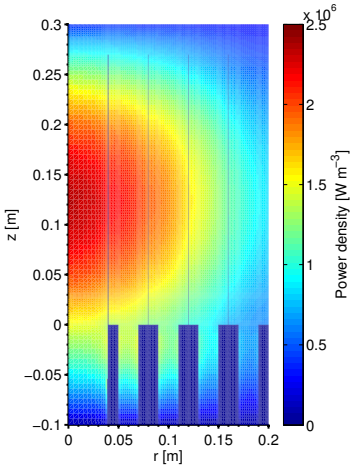

(d) Power density profile

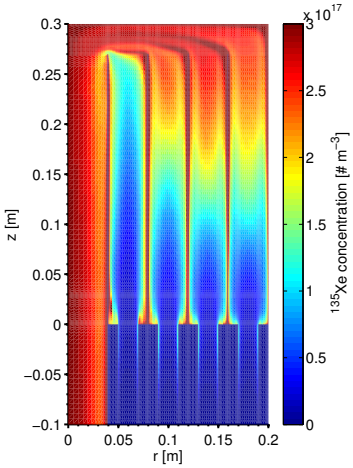

(e) ^{135}Xe concentration profile

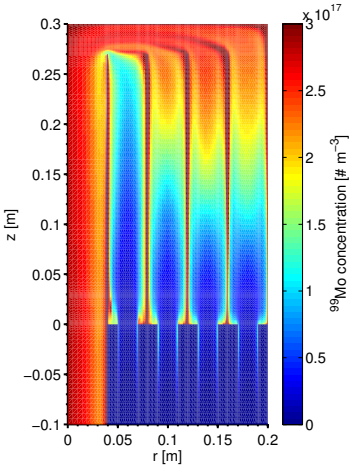

(f) ^{99}Mo concentration profile

Figure 5.8: The velocity vector plot and temperature, pressure, power density and concentration profiles for a mass flow rate of $0.5\,\mathrm{kg\,s^{-1}}$ of the *bulkheads* geometry.

Chapter 6

Safety analysis

In this research, an investigation into three components of the AHR that can fail, namely the heat exchanger, fission products filter and the refueling. Furthermore a reactivity insertion is simulated, which simulates the removal of a control rode. These parts of the loop are not modeled, therefore their failure has an immediately effect on the inlet conditions. Imperial College London[50] simulated only reactivity insertion in their AHR model, however their model uses cooling coils and feedback due to voiding. Pumping failure is not investigated because the designs in this research are such that the reactor vessel will flow empty when the pumps stops. The method used for these transient calculations is described in section 3.3.2.

6.1 Heat exchanger failure

When the heat exchanger fails, the outlet temperature of the AHR will become the inlet temperature. However the fission products filter is still operational. Two values for the mass flow rates, $0.25\,\mathrm{kg\,s^{-1}}$ and $0.50\,\mathrm{kg\,s^{-1}}$, will be assessed to see whether there is a significant difference between the two. When the heat exchanger fails the temperature will raise, this leads to Doppler broadening of the fuel. Therefore more neutrons will be absorbed than produced leading to a decrease of the neutron flux (i.e. power production). The effect of the heat exchanger failure on the total power and the average temperature can be seen in fig. 6.1. Since the transient is slow, relatively long time steps can be used in HEAT (0.1 s). Four temperature profiles have been calculated for different moments in time and are depicted in fig. 6.2. Figure 6.2(d) shows a homogeneous temperature in the fuel and heat loss through the reflector bottom where the boundary condition is specified at 303 K. This is the reason for the decrease of the average temperature in fig. 6.1.

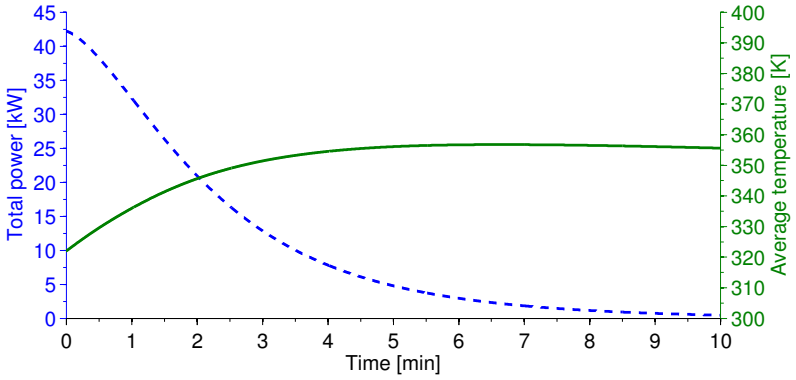

Figure 6.1: The effect of a heat exchanger failure with a mass flow rate of $0.5\,\mathrm{kg\,s^{-1}}$ on the total power(- -) and the average temperature(—) as a function of time. Within 10 minutes, the reactor has a power of 1.15 % of the steady state total power. The maximum local temperature in the system is 367 K and occurs between 3.5 minutes and 5 minutes after the failure started. Hereafter the temperature profile becomes smoother and heat loss trough the bottom occurs (see fig. 6.2(d)).

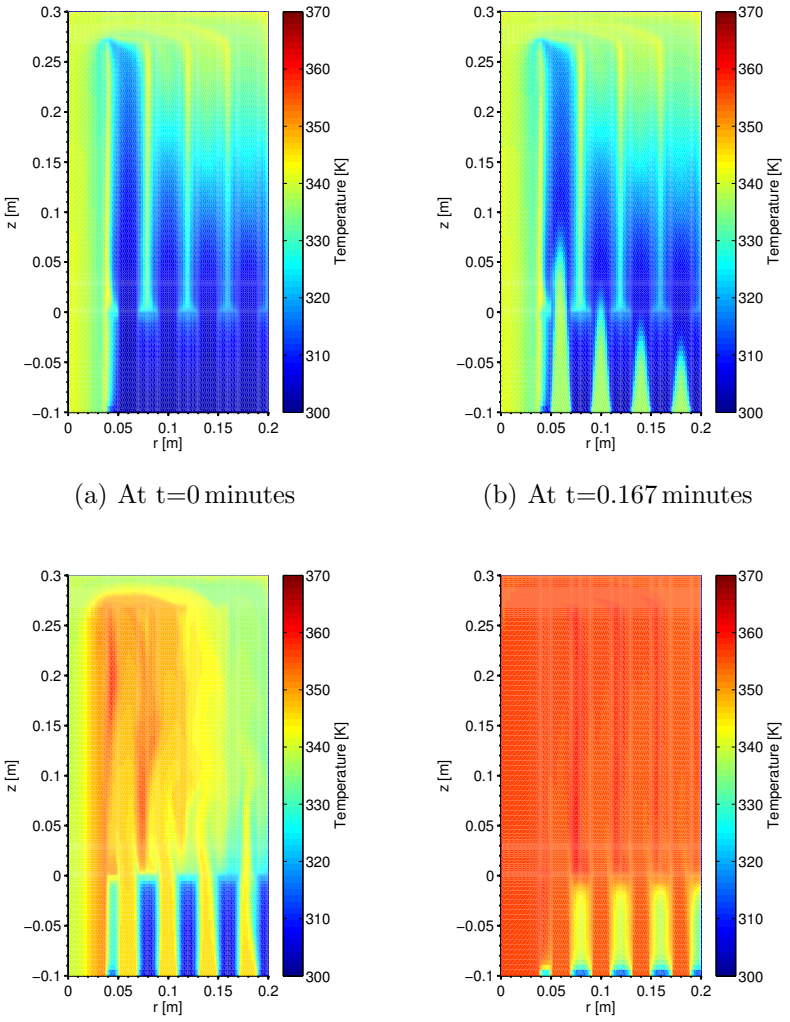

(a) At t=0 minutes

(b) At t=0.167 minutes

(c) At t=1.5 minutes

(d) At t=10 minutes

Figure 6.2: The temperature profiles of the transient of fig. 6.1 at different moments in time. The fuel temperature becomes homogeneous at a certain moment. The maximum local temperature in the system is 367 K and does not exceed the boiling temperature of water. In fig. 6.2(d) heat is only lost through the reflector bottom, the other walls are defined as an insulator.

In order to see the effect of the mass flow rate in case of a heat exchanger failure, a simulation is made for lower mass flow rate of $0.25\,\mathrm{kg\,s^{-1}}$. This is depicted in fig. 6.3. The initial condition of this simulation is the steady state calculation for this mass flow rate, which was calculated in the previous chapter. The initial total power is lower due to the fact that a lower mass flow rate can cool less. The transient is going roughly two times slower, the power after 20 minutes is 1.18 % which is approximately the same percentage as the transient of fig. 6.1.

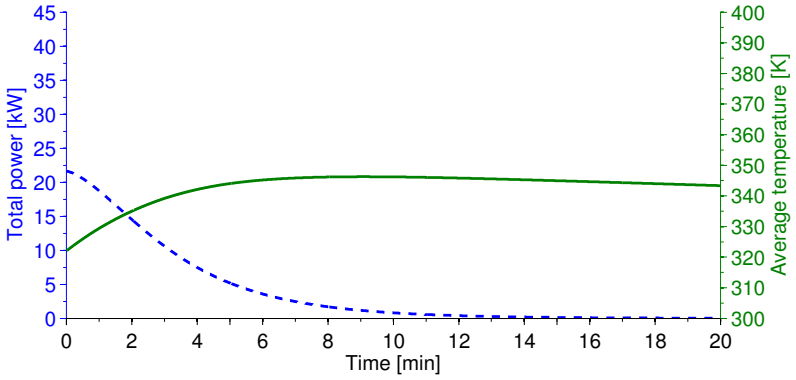

Figure 6.3: The effect of a heat exchanger failure with a mass flow rate of $0.25\,\mathrm{kg\,s^{-1}}$ on the total power(- -) and the average temperature(—) as a function of time. The decrease of the average temperature after 8 minutes is due to heat loss through the bottom of the system.

6.2 Fission products filter failure

When the fission products filter fails the outlet xenon-135 concentration of the filter will become the inlet concentration. The reason only ^{135}Xe is the investigated is the fact that it can be disolved[51] and that it has a high cumulative fission yield. As can be seen in fig. 6.4, the effect of the increasing xenon concentration has a weak impact on the total power. After two hours, the total power is 43 % of the initial value. Since the decay of xenon (n,γ) will equal the production, the total power will reach a new steady state power after several hours (the half-life time of ^{135}Xe is 9.14 hours). This effect is the reason for the flattening of the average xenon concentration curve that occurs after one hour. The time steps taken for HEAT were 0.1 s and for point kinetics 1 µs.

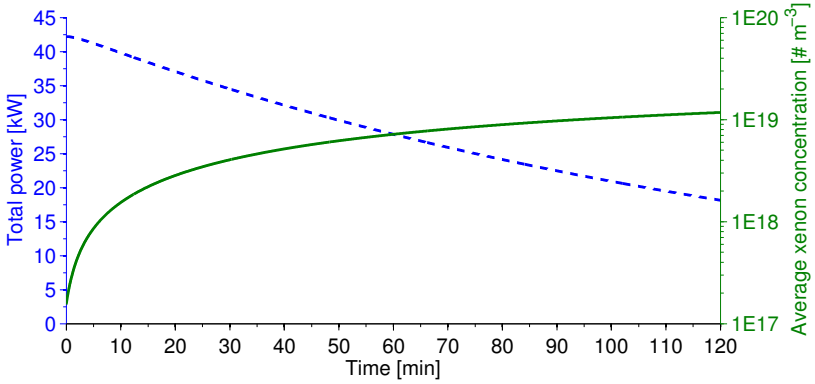

Figure 6.4: The effect of a fission products filter failure with a mass flow rate of $0.50\,\mathrm{kg\,s^{-1}}$ on the total power(- -) and the average xenon concentration(—) as a function of time. The rise of the average xenon concentration will decline, since total power (i.e. the neutron flux) is decreasing over time and a steady state concentration will be reached. *Note the logarithmic axis of the average xenon concentration.*

6.3 Variation of the uranium inlet concentration

In this section the sensitivity of the uranium concentration is assessed. The reactivity feedback coefficient of uranium found in section 5.2 shows a strong feedback on the system. Therefore small variations of the inlet concentration are made to see the effect on the system. The time steps taken for HEAT were 0.1 s and for point kinetics 1 µs.

6.3.1 An increase of the uranium inlet concentration

At first, the inlet concentration is increased with $0.25\,\mathrm{g\,U\,L^{-1}}$, $0.50\,\mathrm{g\,U\,L^{-1}}$, $0.75\,\mathrm{g\,U\,L^{-1}}$ or $1.00\,\mathrm{g\,U\,L^{-1}}$, the initial concentration is $248\,\mathrm{g\,U\,L^{-1}}$. Within six minutes the average concentration is equal to the inlet concentration, as depicted in fig. 6.5. The increased

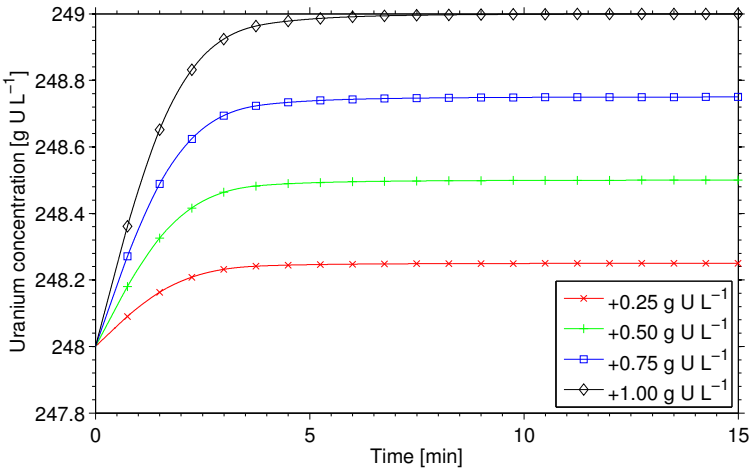

Figure 6.5: The average uranium concentration in the reactor as a function of time for several uranium concentrations increases at t=0 s.

uranium concentration leads to a new steady state total power of respectively 55.7 kW, 69.3 kW, 82.7 kW and 96.2 kW. All new configurations have a maximum power density which is higher than $2.5\,\mathrm{kW\,L^{-1}}$, which is set as the maximum power density for AHRs. The main

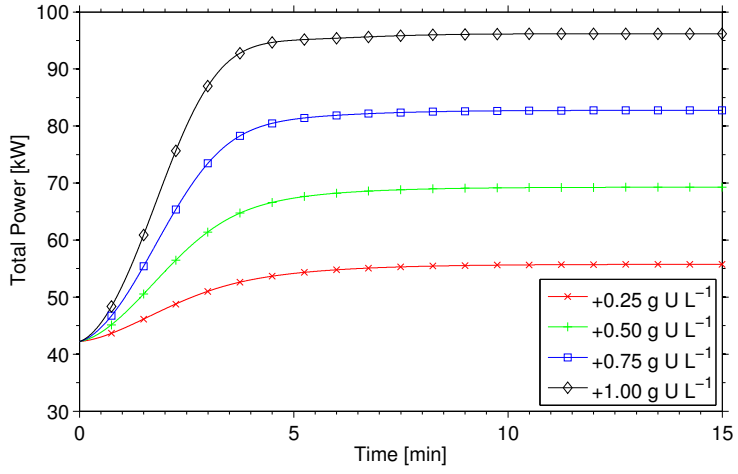

Figure 6.6: The total power of the reactor as a function of time when the uranium concentration was increased at t=0 s.

feedback is provided by the temperature. The average temperatures are depicted in fig. 6.7. However the maximum temperature within the system exceeds the boiling temperature of water for the increased uranium inlet concentration of $+0.75\,\mathrm{g\,U\,L^{-1}}$ and $+1.00\,\mathrm{g\,U\,L^{-1}}$. For the new inlet concentration $248.75\,\mathrm{g\,U\,L^{-1}}$, the maximum local temperature is 380 K and 392 K for an inlet concentration $249\,\mathrm{g\,U\,L^{-1}}$. These results are not fully valid, because the boiling of water is not taken into account.

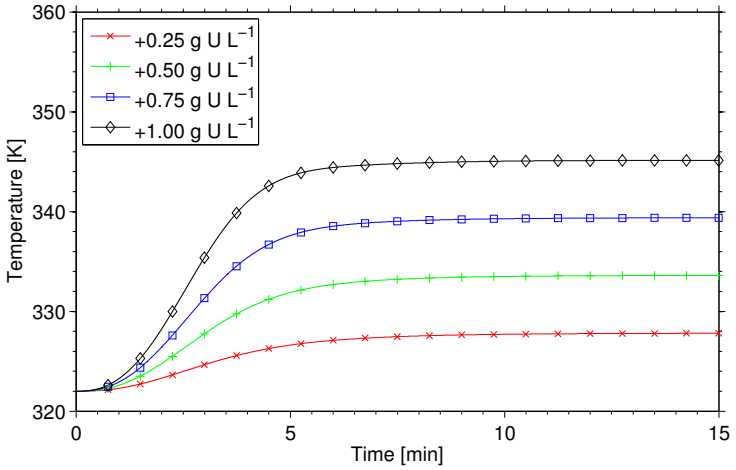

Figure 6.7: The average temperature in the reactor as a function of time due to an increase of the uranium concentration at t=0 s.

6.3.2 A decrease of the uranium inlet concentration

The next step is to decrease the inlet uranium concentration of the reactor with $0.25\,\mathrm{g\,U\,L^{-1}}$, $0.50\,\mathrm{g\,U\,L^{-1}}$, $0.75\,\mathrm{g\,U\,L^{-1}}$ or $1.00\,\mathrm{g\,U\,L^{-1}}$. Here the time needed for reaching the new equilibrium uranium concentration is also around six minutes, as can been seen in fig. 6.8. The reduction of uranium concentration with $0.75\,\mathrm{g\,U\,L^{-1}}$ and $1.00\,\mathrm{g\,U\,L^{-1}}$ leads to a

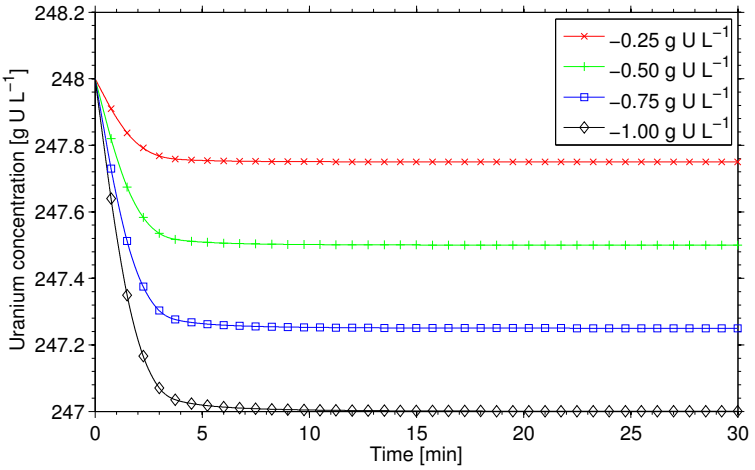

Figure 6.8: The average uranium concentration as a function of time for several uranium concentrations decreases at t=0 s.

subcritical reactor, see figs. 6.9 and 6.10. The temperature of the system will not become lower than 303 K, since this is the set inlet temperature. The temperature has to be

lower than that to compensates for the uranium. The new steady state power for a concentration reduction of $0.25\,\mathrm{g\,U\,L^{-1}}$ is 28.7 kW and 15.4 kW for a concentration reduction of $0.50\,\mathrm{g\,U\,L^{-1}}$.

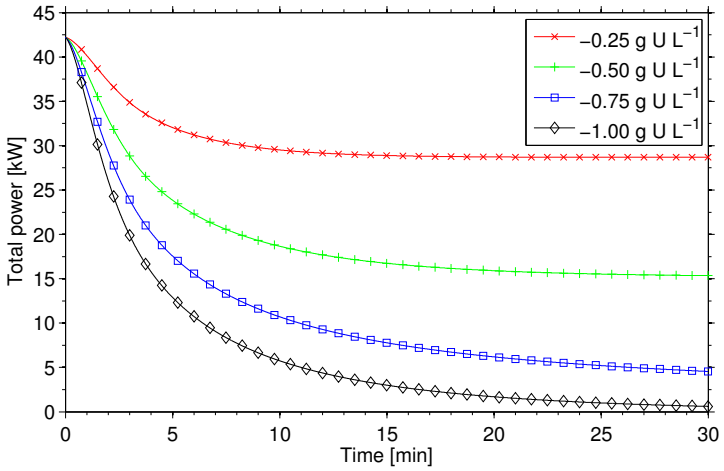

Figure 6.9: The total power of the reactor as a function of time due to a decrease of the uranium concentration at t=0 s.

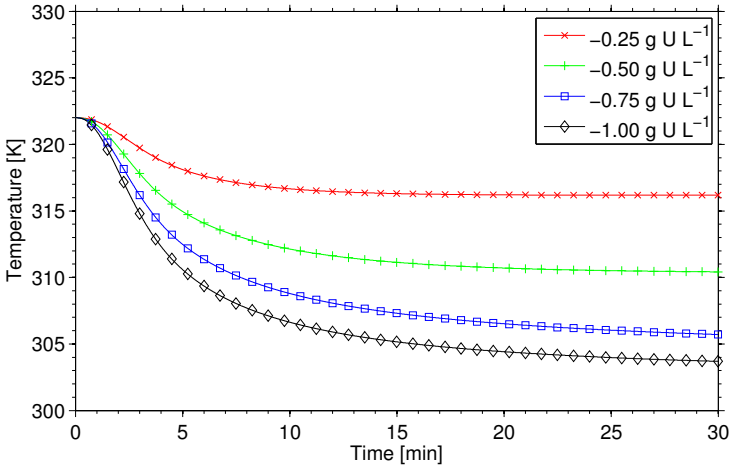

Figure 6.10: The average temperature in the reactor as a function of time due to a decrease of the uranium concentration at t=0 s.

6.4 Reactivity insertion

The reactivity insertions added to the transients of reactivity insertions happen on small time scales. Therefore HEAT was modified to have slowly increasing time steps. An overview of these time steps can be seen in table. 6.1. In total four different insertions were calculated, namely 10 pcm (fig.6.11), 20 pcm (fig.6.12), 40 pcm (fig.6.13) and 60 pcm (fig.6.14).

Table 6.1: Time steps taken for HEAT and point kinetics during a reactivity insertion.

Time frame	**HEAT**	**Point Kinetics**
time $\leq$ 1 ms	1 µs	1 µs
1 ms $<$ time $\leq$ 10 ms	10 µs	1 µs
10 ms $<$ time $\leq$ 100 ms	100 µs	1 µs
100 ms $<$ time $\leq$ 1 s	1 ms	1 µs
1 s $<$ time $\leq$ 10 s	10 ms	1 µs
10 s $<$ time	100 ms	1 µs

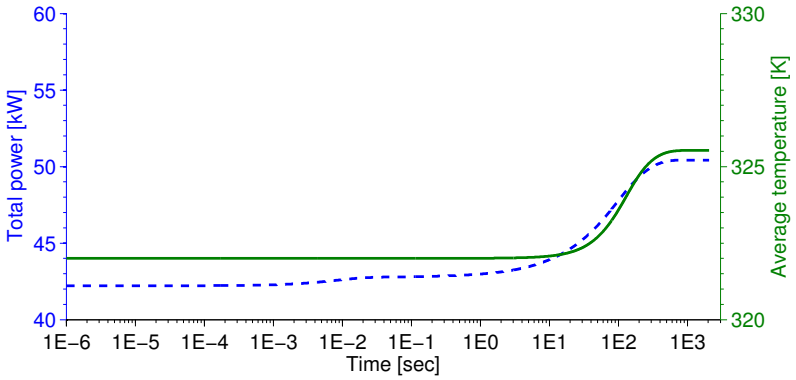

Figure 6.11: The effect of a 10 pcm reactivity insertion with a mass flow rate of 0.50 kg s^{-1} on the total power(- -) and the average temperature (—) as a function of time. The new steady state total power is 50.4 kW with an average temperature of 325.5 K and the maximum local temperature in the system during the transient is 351 K.

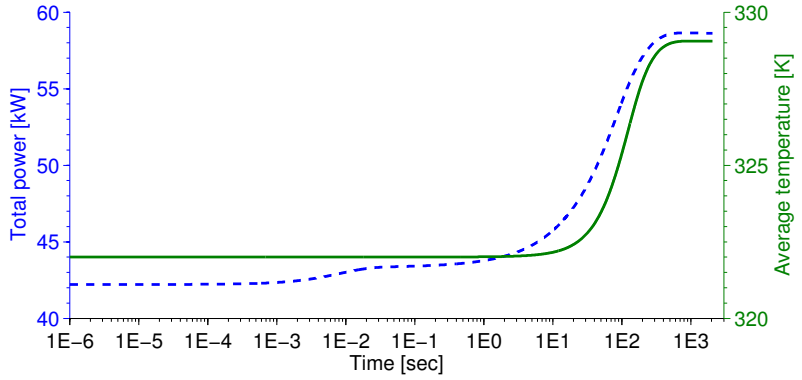

Figure 6.12: The effect of a 20 pcm reactivity insertion with a mass flow rate of $0.50\,\mathrm{kg\,s^{-1}}$ on the total power(- -) and the average temperature (—) as a function of time. The new steady state total power is 58.6 kW with an average temperature of 329.1 K and the maximum local temperature in the system during the transient is 358 K.

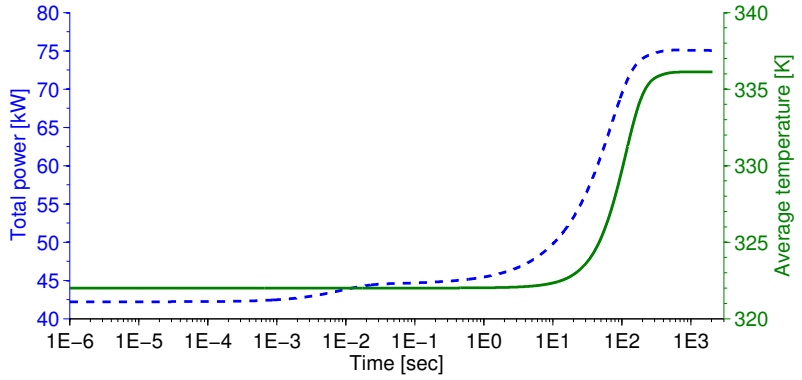

Figure 6.13: The effect of a 40 pcm reactivity insertion with a mass flow rate of $0.50\,\mathrm{kg\,s^{-1}}$ on the total power(- -) and the average temperature (—) as a function of time. The new steady state total power is 75.0 kW with an average temperature of 336.1 K and the maximum local temperature in the system during the transient is 373 K.

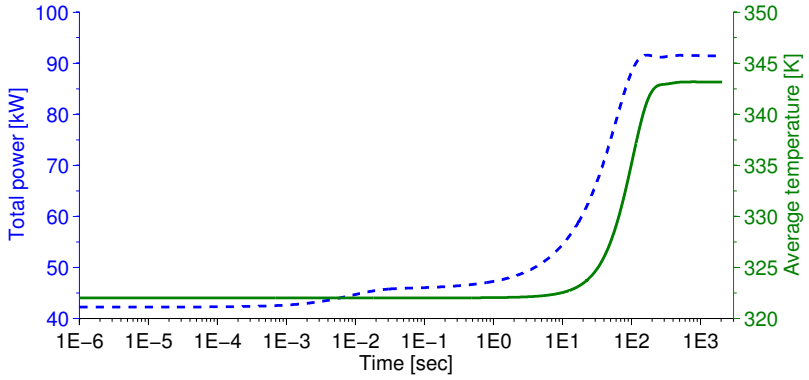

Figure 6.14: The effect of a 60 pcm reactivity insertion with a mass flow rate of $0.50\,\mathrm{kg\,s^{-1}}$ on the total power(- -) and the average temperature (—) as a function of time. The new steady state total power is 91.4 kW with an average temperature of 343.1 K and the maximum local temperature in the system during the transient is 388 K.

The system is sensitive for a reactivity insertion of 40 pcm or 0.05 \$, it is already enough to get the system locally at boiling temperature. Therefore the results of the transient of the 40 pcm are just valid, but those of the 60 pcm insertion are physically incorrect due to fact that the temperature exceeds locally the boiling point of water. The feedback is predominantly given by temperature, for instance the average xenon contraction for the 60 pcm insertion is doubled during the transient, but gives a feedback of only -0.4 pcm (see fig. 6.15).

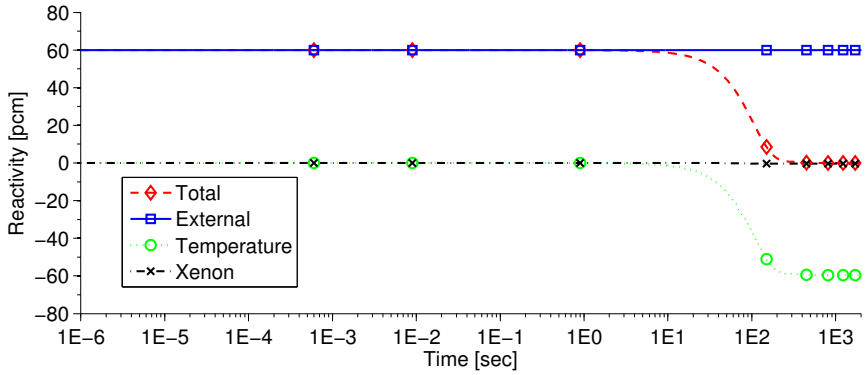

Figure 6.15: A trace of the reactivity during insertion of 60 pm. The feedback predominantly given by the temperature.

Chapter 7

Conclusions

7.1 Conclusions

In this thesis an initial study has been done on the possibility of using a small sized Aqueous Homogeneous Reactors (AHR) as a tool to produce medical isotopes. AHRs show good potential for such purposes due to the fact that the irradiation and filtering are done in a single device. Past experience of the few operated AHRs show that the reactor can run for long periods of time, like the SUPO reactor and Argos reactor. The conclusion are summarized into three categories, namely the fuel, the geometry and the safety. Which are the main topics investigated during this research.

Fuel

In order to ensure that the concentration of the uranium salt does not exceed the solubility, the uranium should be enriched to 20 %. A literature study showed that uranyl nitrate is the most suitable uranium salt for the production of molybdenum-99 (^{99}Mo), as ^{99}Mo is extracted more efficiently from uranyl nitrate than from uranyl sulphate. The highest yield of ^{99}Mo is extracted when the extraction happens continuously. For this method the fuel has to be pumped around, therefore it is convenient to place the heat exchanger in the same loop.

Geometry

Since the fuel is pumped trough the reactor, a suitable geometry has to be found for spreading heat equally. The best performing geometry was the so called *Bulkheads* geometry, which consists of four inlets, one outlet and four vertical walls (*Bulkheads*) for directing flow upward. The benefit of this configuration is the smooth flow of the fuel through the system. Furthermore no obstruction for the radiolytic gases is present. Initially the original single inlet had hot spots and vortexes. The drawback of this extra structural material is the fact that radiolytic gases will get trapped in the reactor (depending on the design).

The maximum mass flow rate for the *Bulkheads* geometry is $0.5\,\mathrm{kg\,s^{-1}}$. If the mass flow rate is increased, the maximum power density exceeds $2.5\,\mathrm{kW\,L^{-1}}$. A higher mass flow rate leads to more cooling due to the negative temperature feedback as well as a higher total power and power density. This power density is set to be the limit for future AHR. The weekly ^{99}Mo production of the system is 309 6-day Ci, which is roughly 2.5 % of the world demand.

Safety

The *Bulkheads* geometry obeys two of the three characteristics of an AHR mentioned in the introduction, namely the small size and the small total power. The calculated temperature feedback coefficient is much lower than reported in literature for similar systems. This may be due to various causes like different temperature, concentration, enrichment and fuel type or the fact that the density of uranyl does dependent on temperature. In this research

the temperature only led to Doppler broadening. Due to the low temperature feedback coefficient, the system is very sensitive to the small uranium concentration and reactivity insertions. Because the system uses water under atmospheric pressure, the temperature range is limited and the feedback given by temperature difference is also limited. Despite this, a failure of the heat exchanger or the fission product filter do not lead to boiling of the water inside the reactor. Since the total power (42.2 kW) of the reactor is relatively low, the consumption of uranium is marginal and the system can be operated for longer periods without feeding new uranium into the system. Therefore the risk of adding to much uranium nitrate to solution can be reduced, since only a few grams is needed.

In conclusion, the weekly production of ^{99}Mo shows the potential of a small sized AHR as a way for producing medical isotopes. Furthermore, the safety analysis done on the *Bulkheads* geometry demonstrates that the system is stable.

7.2 Future directions

Future research can be divided into different areas, namely material properties, geometry and computational modeling.

Currently material properties of uranyl nitrate, uranyl sulphate and uranyl fluoride are only available for some concentrations, temperatures and acidity of the fluid. In order to have more accurate results, parameters such as dynamic viscosity and thermal expansion coefficient need to be known for the uranium salts. Besides, more information about the fuel properties also the effect of a low pH-level and the neutron flux on the structural materials should be investigated. Thereby ensuring no leaks will appear. In this research the decision was made to use uranyl nitrate, however uranyl sulphate still has potential to be used as fuel, since no nitrogen gases are formed. A more detailed research should be done in the advantages and disadvantages of the two uranium salts.

The assessed geometry with the multiple inlets (*Bulkheads* geometry) has an outflow pipe in the center of the cylindrical reactor. One could study effect of varying the inlet position to see whether this enhanced the heat removal.

In order to extend the model, the boiling phenomena and radiolysis the computational fluid code should be extended to a multiphase code. These effects enhance the safety of the reactor, because they provide negative feedback to the system. Furthermore the code can be extended to include blockage of the outflow pipe, this is a transient initiator with possibly large consequences.

The transport code used for this research is Serpent 2.1.12. The input files needed for Serpent are easy to produce and do not require a long learning process. However in Serpent the fuel is considered to be stationary, which is valid for light water reactors, but not for an AHR. An in-house written diffusion code (DALTON-MSR) can be modified to be used for an AHR. This code is able to take into account the convection of the precursor. Furthermore the coupling of DALTON-MSR with HEAT provides a better calculation of the transient.

In this thesis only the production of molybdenum-99 was assessed, since it is the most commonly used medical isotope. Other isotopes, for instance ^{131}I is used for the treatment of thyroid cancer, can or might also be produced within an AHR. The current model assumes a 100 % yield of the filters. One can study the effect of a non-perfect filter, since ^{99}Mo can also absorb neutrons, thereby reducing the production yield.

Acknowledgments

I would like to thank Zoltan Perko for the numerous useful discussions. Thanks goes to my supervisors Jan-Leen Kloosterman and Martin Rohde for their guidance during the project and to Danny Lathouwers for getting a better understanding and some debugging of the HEAT code. I also would like to thank PhD- and MSc-students Luca, Stuart, Gert-Jan, Bart, Frank, Valentina , Johan, Dirk-Jan, Dick, Lodewijk and Wilhelm for providing a great athmosphere during my time at NERA. Last and certainly not least, I would like to thank Lars Bannenberg for proofreading my thesis.

Bibliography

[1] Elfrida Saragi Topan Setiadipura. Neutronic aspect of Subcritical Assemby for Mo-99 Production (SAMOP) Reactor. *International Conference on Advances in Nuclear Science and Engineering*, page 1, 2007.

[2] Annex to the IAEA's Nuclear Technology Review 2010 . Production and Supply of Molybdenum-99. *Nuclear Technology Review*, September 2010.

[3] Paula Gould. Medical isotope supplies dwindle, 2013. http://nauka.in.ua/en/news/articles/article_detail/4996.

[4] R.M. Ball. Testimony before the congressional committee on U.S resources on the production of Mo-99 with Aqueous Homogeneous Reactors. *Mike Synar*, 1992.

[5] R.M. Ball. Medical isotope production reactor. January 1997. patent:5596611 `http://www.freepatentsonline.com/5596611.html`.

[6] Feasibility evaluation of the use of low enriched uranium fuelled homogeneous aqueous solution nuclear reactors for the production of short lived fission product isotopes. 2010.

[7] Merle E. Bunker. Early reactors — from Fermi's water boiler to novel power prototypes. *Los-Alamos-Science*, 7:124–131, 1983.

[8] John R. Ireland. Design Principals for Aqueous Homogeneous Reactors. *Mo99 Topical Meeting*, 2011. LA-UR 11-06788.

[9] A.G. Buchan, C.C. Pain, A.J.H. Goddard, M.D. Eaton, J.L.M.A. Gomes, G.J. Gorman, C.M. Cooling, B.S. Tollit, E.T. Nygaard, D.E. Glenn, and P.L. Angelo. Simulated transient dynamics and heat transfer characteristics of the water boiler nuclear reactor {SUPO} with cooling coil heat extraction. *Annals of Nuclear Energy*, 48(0):68 – 83, 2012.

[10] KEMA. *Final Report on the Aqueous Homogeneous Suspension Reactor Project*. KEMA scientific & technical reports. KEMA, 1987. ISBN 9789035300484.

[11] We E. Parkins, R. F. Wilson, W0 No McElroy, J. 0. Henry, and Williams R. 0. Aqueous Homogeneous type Research Reactors. *Second United Nations International Conference on the Peaceful Uses of Atomic Energy*, pages 1–18, March 1958.

[12] Murray W. Rosenthal. An Account of Oak Ridge National Laboratorys Thirteen Nuclear Reactors. March 2010. ORNL/TM-2009/181.

[13] Steven K. Klein. Mo-99 Production Technology Development at LANL. *Los Alamos National Laboratory Advanced Nuclear Technology Group*, pages 1–37, 2011.

[14] Robert Kimpland. SHEBA prompt burst dynamics. *Los Alamos National Laboratory Advanced Nuclear Technology Group*, pages 1–9, 1997.

[15] C.C. Cappiello, K.B. Butterfield, and R.G. Sanchez. Solution High-Energy Burst Assembly (SHEBA) results from subprompt critical experiments with uranyl fluoride fuel. *Los Alamos National Laboratory*, pages 1–9, 1997.

[16] Akio Ono. Solution Behavior Visualization System for the Development of a Criticality Accident Case. Website, June 2000. http://www.jaea.go.jp/jaeri/english/press/000629/index.html.

[17] Francis Barbry. French CEA Experience on homogeneous Aqueous Solution Nuclear Reactors. *I.A.E.A. Consultancy Meeting*, pages 1–21, 2007.

[18] D.Yu. Chuvilin, V.E. Khvostionov, D.V. Markovskij, V.A. Pavshook, N.N. Ponomarev-Stepnoy, A.N. Udovenko, A.V. Shatrov, Yu. I. Vereschagin, J. Rice, and L.A. Tome. Production of 89Sr in solution reactor. *Applied Radiation and Isotopes*, 65(10):1087 – 1094, 2007.

[19] Valentin Ivanov. Research reactors in Russia. status and prospects for reducing the fuel enrichment. page 14, 2010.

[20] V.A. Pavshook and V.Ye.Khvostionov. Present status of the use of LEU in aqueous reactors to produce Mo-99. page 5, 1998.

[21] Yu.D. Baranaev, V.A. Pivovarov N.A. Nerozin and, and E.Ya. Smitanin. Medical Complex for Radioisotopes Production. In *Assessment of utility of Homogeneous Aqueous Solution Nuclear Reactors for the production of Mo-99 and other short-lived radioisotopes*, June 2007.

[22] X. SONG and W. NIU. Optimization of 200kW Medical Isotope Production Reactor Design. *Sichuan Nuclear Society*, pages 1–7, 2000.

[23] Tegas Sutondo, Syarip, and Slamet Santoso. Safety Design Limits of Main Components of The Proposed SAMOP System. *Asian Physics Symposium*, pages 403–406, 2009.

[24] Topan Setiadipura and Elfrida Saragi. Neutronic aspect of Subcritical Assemby for Mo-99 Production (SAMOP) Reactor. In *ICANSE in conjunction with LKSTN XVIII*, June 2007.

[25] W.E. Reynolds. IAEA Consultancy on Aqueous Homogeneous Reactors for the Production of Mo-99. In *Assessment of utility of Homogeneous Aqueous Solution Nuclear Reactors for the production of Mo-99 and other short-lived radioisotopes*, June 2007.

[26] T. A. Policke, D. E. Glenn, S. B. Aase, D. Amaya, and V. Wilkinson. INVAP/B&W Mini-Loop Production of Mo-99. In *1st ANNUAL MOLYBDENUM-99 TOPICAL MEETING*, 2011.

[27] Suzanne Kitten and Charlene Cappiello. Solution-reactor-produced Mo-99 using activated carbon to remove I-131. *Los-Alamos-Science*, 7:102–103, 1998.

[28] G.W. Neeley. Design Aspects Of A Solution Reactor For The Production Of Mo-99. In *Assessment of utility of Homogeneous Aqueous Solution Nuclear Reactors for the production of Mo-99 and other short-lived radioisotopes*, June 2007.

[29] Nuclear non-proliferation treaty — wikisource, 2013. http://en.wikisource.org/w/index.php?title=Nuclear_Non-Proliferation_Treaty&oldid=4383354.

[30] Nuclear Fuel Cycle and Materials Section. Homogeneous Aqueous Solution Nuclear Reactors for the Production of Mo-99 and other Short Lived Radioisotopes. *IAEA*, page 2, September 2008.

[31] W. C. de Baat. Sur l'acide dithionique et ses sels. *Recueil des Travaux Chimiques des Pays-Bas*, 45(4):237–244, 1926.

[32] J.A. Lane, U.S. Atomic Energy Commission, and International Conference on the Peaceful Uses of Atomic Energy. *Fluid fuel reactors. Edited by James A. Lane, H.G. MacPherson [and] Frank Maslan.* Addison-Wesley Pub. Co. Reading, Mass.,, 1958. xxii, 979 p. pp.

[33] T.A. Fox and and R.A. Mueller and D. Fieno. Criticality study of NASA solution reactors with 25.4 cm diameter cylindrical stainless steel tanks. September 1971.

[34] Tayyab Mahmood and Masood Iqbal. Optimization study and neutronic design calculations of {LEU} fuelled homogeneous aqueous solution nuclear reactors for the production of short lived fission product isotopes. *Annals of Nuclear Energy*, 42(0):175 – 178, 2012.

[35] Li Maoliang and Cheng Zuoyong and Deng Qimin. The Progress Report of Aqueous Homogeneous Reactor for Medical Isotope Production in China. *NPIC*, pages 1–3, 2007.

[36] D.J. Diamond, S. Bajorek, A. Bakel, G. Flanagan, V. Mubayi, R. Skarda, J. Staudenmeier, T. Taiwo, K. Tonoike, C. Tripp, T. Wei, and P. Yarsky. Aqueous Homogeneous Reactor Technical Panel Report. *Brookhaven National Laboratory*, 2010.

[37] V.A. Pivovarov. Institute for Physics and Power Engineering, Presentation at the IAEA 2007 consultant meeting. February 2010.

[38] VTT Technical Research Centre. Serpent - a monte carlo reactor physics burnup calculation code. http://montecarlo.vtt.fi/.

[39] Versteeg, H.H.K. and Malalasekera, W. *An Introduction to Computational Fluid Dynamics: The Finite Volume Method.* Pearson/Prentice Hall, 2007. ISBN 9780131274983. LCCN 2006052528.

[40] Patankar, S.V. *Numerical heat transfer and fluid flow.* Series in computational methods in mechanics and thermal sciences. Hemisphere Pub. Corp., 1980. ISBN 9780070487406. LCCN 79028286.

[41] E. van der Linden. Coupled neutronics and computational fluid dynamics for the molten salt fast reactor. 2012. PNR-131-2012-005.

[42] K.O. Ott and R.J. Neuhold. *Introductory nuclear reactor dynamics.* American Nuclear Society, 1985. ISBN 9780894480294. LCCN 85022903.

[43] L.P.B.M. Janssen and C.G. Warmoeskerken. *Transport Phenomena Data Companion.* Edward Arnold, 1987. ISBN 9780713136180.

[44] Barbry, Francis. French solution reactor experience and contribution to the Feasibility of the Use of LEU Fuelled Homogenous Aqueous Solution Nuclear Reactors for the Production of Short Lived Fission Product Isotopes. 2010. IAEA CRP / RCM 22-26.

[45] United Performance Metals. 304 / 304l stainless steel sheet & coil - physical. http://www.upmet.com/products/stainless-steel/304304l-ann/physical.

[46] Japan Atomic Energy Agency. Nuclide information 42-mo-99. http://wwwndc.jaea.go.jp/cgi-bin/nuclinfo2010a.cgi?42,99.

[47] Japan Atomic Energy Agency. Nuclide information 54-xe-135. http://wwwndc.jaea.go.jp/cgi-bin/nuclinfo2010a.cgi?54,135.

[48] C. TJoen and M. Rohde. Experimental study of the coupled thermo-hydraulicneutronic stability of a natural circulation {HPLWR}. *Nuclear Engineering and Design*, 242(0): 221 – 232, 2012.

[49] P.R. Kasten, Oak Ridge National Laboratory. Reactor Experimental Engineering Division, Union Carbide Nuclear Company, and U.S. Atomic Energy Commission. *Operational safety of the homogenous reactor test.* Oak Ridge National Laboratory, 1956.

[50] C.M. Cooling, M.M.R. Williams, E.T. Nygaard, and M.D. Eaton. The application of polynomial chaos methods to a point kinetics model of mipr: An aqueous homogeneous reactor. *Nuclear Engineering and Design*, 262(0):126 – 152, 2013.

[51] A. von Antropoff. The solubility of xenon, krypton, argon, neon, and helium in water. *Proceedings of the Royal Society of London. Series A, Containing Papers of a Mathematical and Physical Character*, 83(565):pp. 474–482, 1910.

[52] Tegas Sutondo. Analytical method of atomic density determination of the uranyl nitrate solution system. *A Calculation Note, Part of Neutronic Design Analysis of SAMOP System.*

[53] J.R. de Laeter, International Union of Pure, and Applied Chemistry. *Atomic Weights of the Elements: Review 2000 : IUPAC Technical Report.* Pure and applied chemistry. 2003.

[54] P.J.B. Hakkinen, A. Mohapatra, S.G.G. Gilbert, and P. Wexler. *Information Resources in Toxicology.* Elsevier Science, 2009. ISBN 9780123735935.

[55] Flinn Scientific Inc. Material safety data sheet # 839.10, 2001. http://www.mnps.org/AssetFactory.aspx?did=58683.

[56] International Bio-Analytical Industries Inc. Uranyl fluoride msds. http://www.ibilabs.com/Uranyl%20Flouride-MSDS.htm.

Appendix A

Particle density calculation

In subsection 2.1.4, the particle density is calculated using the method of Tegas[52]. The paper itself is in Indonesian and the method below is slightly different than Tegas' method. The isotope mass and densities that have been used are listed in table A.1 and A.2.

Table A.1: An overview of the relevant masses of isotopes[53].

Material	**Isotope mass** $[\mathrm{g\,mol^{-1}}]$
^{1}H	1.00794
^{14}N	14.0067
^{16}O	15.9994
^{19}F	18.9984032
^{32}S	32.065
^{234}U	234.040952088
^{235}U	235.0439299
^{238}U	238.05078826
H_2O	18.0153

Table A.2: Density of the different fuels.

Material	**Density** $[\mathrm{g\,cm^{-3}}]$	**Ref.**
UO_2SO_4	3.28	[54]
$UO_2(NO_3)_2$	2.807	[55]
UO_2F_2	6.45	[56]
H_2O	1	[43]

When uranium is enriched, the mass fraction of both U_{235} and U_{234} are increased. To model this, Tegas used the mass fraction of natural uranium and that of 3.5% enriched uranium (see tab. A.3). By applying a linearization based on these two data points an estimation can be made for higher enrichments.

Table A.3: Mole fraction of natural uranium and 3.5% enrich uranium[52].

Isotope	**Natural uranium [%]**	**3.5 % enrich uranium[%]**
^{234}U	0.0053	0.02884
^{238}U	0.711	3.5
^{238}U	99.284	96.471

This leads to the following expression for the mass fraction of U_{234}:

$$w_{234} = 8.44 \cdot 10^{-3} w_{235} - 7.0084 \cdot 10^{-4}, \tag{A.1}$$

where w_{235} is the enrichment of U_{235}. The mass fraction of U_{238} becomes:

$$w_{238} = 100\% - (w_{234} + w_{235})\,. \tag{A.2}$$

The particle density can be calculated using the following equations:

$$N_{^{234}U} = \frac{w_{234} w_u}{A_{234}} N_A, \tag{A.3}$$

$$N_{^{235}U} = \frac{w_{235} w_u}{A_{235}} N_A, \tag{A.4}$$

$$N_{^{238}U} = \frac{w_{238} w_u}{A_{238}} N_A, \tag{A.5}$$

where w_u is the amount of uranium dissolved in water ($\mathrm{g\,U\,L^{-1}}$), A_i is the isotope mass (see tab. A.1) and N_A is Avogadro's number ($6.022\,141\,29 \times 10^{23}\,\mathrm{mol^{-1}}$ [43]). The total mass of the dissolved fuel is:

$$w_{fuel} = \sum_i w_i = \sum_i \frac{N_{iU} B_i}{N_A}, \tag{A.6}$$

where the summation is over the uranium isotopes, N_{iU} is the particle density and B_i the atomic mass unit of the molecule, e.g. uranyl nitrate. The last step is to calculate the number of hydrogen and oxygen atoms that are present in the water. The volume that is occupied by the water is:

$$V_{water} = 1000\,\mathrm{cm^3} - V_{fuel}, \tag{A.7}$$

The volume of $1000\,\mathrm{cm^3}$ comes from the fact that a volume of $1\,\mathrm{L}$ is used to solve the densities. The volume of the fuel can be calculated using:

$$V_{fuel} = \frac{w_{fuel}}{\rho_{fuel}}. \tag{A.8}$$

The density, ρ_{fuel}, can be found in tab. A.2. The particle density of hydrogen and oxygen are:

$$N_H = 2\frac{V_{water}\rho_{water}}{A_{water}} N_A, \tag{A.9}$$

$$N_O = \frac{V_{water}\rho_{water}}{A_{water}} N_A. \tag{A.10}$$

The average density can be calculated using:

$$\rho_{avg} = \frac{\rho_{fuel} V_{fuel} + V_{water}\rho_{water}}{V_{fuel} + V_{water}}. \tag{A.11}$$

Nomenclature

General acronyms

AHR	Aqueous Homogenous Reactor
AHSR	Aqueous Homogeneous Solution Reactor
B&W	The Babcock & Wilcox Company
BATAN	Badan Tenaga Nuklir Nasional National Nuclear Energy Agency of Indonesia
BR-2	Belgian Reactor 2 in Mol, Belgium
CEA	Commissariat à l'Énergie Atomique
CFD	Computational Fluid Dynamics
ENDF	Evaluated Nuclear Data File
HASR	Homogeneous Aqueous Solution nuclear Reactors
HAR	Homogeneous Aqueous Reactor
HFR	High Flux Reactor in Petten, the Netherlands
HEU	High Enrich Uranium
HYPO	High POwer reactor at LANL
HRT	Homogeneous Reactor Test at ORNL
IPPE	Institute of Physics and Power Engineering
KEMA	Keuring van Elektrotechnische Materialen te Arnhem (Inspection of Electrotechnical Materials in Arnhem)
LANL	Los Alamos National Laboratory in Los Alamos, New Mexico, USA
LEU	Low Enrich Uranium
LOPO	LOw POwer reactor at LANL
MIPR	Medical Isotope Production Reactor
MIPS	Medical Isotope Production System
NRU	National Research Universal Reactor in Chalk River, Canada
NUCEF	Nuclear Fuel Cycle Safety Engineering Research Facility
OPAL	Open-pool Australian lightwater reactor in Sydney, Australia
ORNL	Oak Ridge National Laboratory in Oak Ridge, Tennessee, USA
SAMOP	Subcritical Assembly for Mo-99 Production at BATAN
SHEBA	Solution High-Energy Burst Assembly at LANL
SR	Solution Reactor
SR-RN	Solution Reactor Radio Nuclides
SUPO	SUper POwer reactor at LANL
TRACY	TRAnsient experiments Critical facilitY

Isotopes and molecules acronyms

F	Fluoride
H	Hydrogen
I	Iodine
Mo	Molybdenum
N	Nitrogen
O	Oxygen
Pu	Plutonium
S	Sulfur
Sr	Strontium
Tc	Technetium
U	Uranium
UO_2SO_4	Uranyl sulphate
$UO_2(NO_3)_2$	Uranyl nitrate
UO_2F_2	Uranyl fluoride
Xe	Xenon

Symbols

A_i	Lateral surface of the inlet [m^2]
C	Scalar value of Serpent OR HEAT mesh cell [–]
C	Concentration [$\# m^{-3}$]
C_p	Specific heat [$J kg^{-1} K^{-1}$]
C_k	Precursor density [–]
$C_{^{235}U}$	^{235}U concentration [$\# cm^{-1} b^{-1}$]
D	Diffusion coefficient [$m^2 s^{-1}$]
E	Energy of a neutron [eV]
$\vec{F_b}$	Gravity force [$kg m^{-2} s^{-1}$]
$F_r(i,j)$	Fraction of each Serpent cell radially difference squared for HEAT radially difference squared [–]
$F_z(i,j)$	Fraction of each Serpent cell height difference for HEAT height difference [–]
g	Gravitational constant [$m s^{-2}$]
p	Pressure [Pa]
P	Power density [$W m^{-3}$]
p	Power amplitude function [–]
$r(i)$	Radius of the mesh cell [m]
$\vec{r}$	Spacial dependence [m]
S	Isotope production density [$\# m^{-3} s^{-1}$]
t	Time [s]

T	Temperature [K]
$\vec{v}$	Velocity [$\mathrm{m\,s^{-1}}$]
V	Volume of a Serpent detector [$\mathrm{m^3}$]
V_i	Volume of a Serpent mesh cell that lies inside a certain HEAT mesh cell [$\mathrm{m^3}$]
w_i	Weight of the inlet mass flow rate [–]
γ	Cumulative fission yield [–]
α	Fit parameter [–]
β	Fit parameter [–]
β	Thermal expansion coefficient [$\mathrm{K^{-1}}$]
β	Effective delay neutron fraction [–]
γ	Fit parameter [–]
$\Delta z(i)$	Height HEAT cell [m]
$\Delta z(j)$	Height of Serpent cell which is inside HEAT cell [m]
phi	Neutron flux [$\mathrm{n\,cm^{-2}\,s^{-1}}$]
Λ	Generation time [s]
λ	Precursor decay constant [s]
λ	Thermal conductivity [$\mathrm{W\,m^{-1}\,K^{-1}}$]
μ	Dynamic viscosity [$\mathrm{m^2\,s^{-1}}$]
ρ	Density [$\mathrm{kg\,m^{-3}}$]
ρ	Reactivity [–]
$\Sigma_{f_{tot}}$	The total fission cross section [$\mathrm{cm^{-1}}$]
τ	Decay constant [s]

Subscripts and superscripts

avg	Average value
ext	External
f	Delayed family
H	HEAT cell
i	Serpent spatial discretization index
in	Inner radius
j	HEAT spatial discretization index
out	Outer radius
ref	Reference value
rel	Relative value
S	Serpent cell